



HAL
open science

Al-Ti-W alloys deposited by magnetron sputtering: Effective barrier to prevent steel hydrogen embrittlement

Issam Lakdhar, Akram Alhussein, Julien Capelle, Juan Creus

► **To cite this version:**

Issam Lakdhar, Akram Alhussein, Julien Capelle, Juan Creus. Al-Ti-W alloys deposited by magnetron sputtering: Effective barrier to prevent steel hydrogen embrittlement. Applied Surface Science, 2021, 567, pp.150786. 10.1016/j.apsusc.2021.150786 . hal-03565074

HAL Id: hal-03565074

<https://utt.hal.science/hal-03565074>

Submitted on 22 Aug 2023

HAL is a multi-disciplinary open access archive for the deposit and dissemination of scientific research documents, whether they are published or not. The documents may come from teaching and research institutions in France or abroad, or from public or private research centers.

L'archive ouverte pluridisciplinaire **HAL**, est destinée au dépôt et à la diffusion de documents scientifiques de niveau recherche, publiés ou non, émanant des établissements d'enseignement et de recherche français ou étrangers, des laboratoires publics ou privés.



Distributed under a Creative Commons Attribution - NonCommercial 4.0 International License

Al-Ti-W alloys deposited by magnetron sputtering: effective barrier to prevent steel hydrogen embrittlement

Issam LAKDHAR^{1,*}, Akram ALHUSSEIN^{1,**}, Julien CAPELLE², Juan CREUS³

¹*LASMIS, Université de Technologie de Troyes, Pôle Technologique Sud Champagne, 26 rue Lavoisier, 52800 Nogent, France.*

²*ENIM, Ecole Nationale d'Ingénieur de Metz, 1 Route d'Ars Laquenexy, 57078 Metz, France.*

³*LaSIE, UMR 7356 CNRS, La Rochelle Université, Av. Michel Crépeau, F-17042 La Rochelle, France.*

Corresponding authors : *I. Lakdhar ; issam.lakdhar@utt.fr

**A. Alhussein ; akram.alhussein@utt.fr

Abstract

Thin film represents a promising alternative for the protection of metallic structures against hydrogen embrittlement and corrosion degradation. Al-Ti-W coatings were deposited by magnetron sputtering technique using three pure metallic targets. Tungsten was incorporated in Al-Ti amorphous coating with different contents ranging from 0 to 17 at% by keeping a constant Ti/Al ratio at an average of 0.8. The deposition rate was calculated in order to obtain 4 μm as an uniform film thickness. XRD, DSC and TEM analyses were performed to confirm the amorphous state of the coatings and to determine the glass transition temperature (T_g) and crystallization temperature peak (T_p). These temperatures were increased respectively from 423°C and 595°C to 490°C and 665°C with the increase of W concentration up to 17 at%. Corrosion resistance in a saline solution decreased with the increase of W content. The incorporation of W element induced an increase of the thin film hardness (H) and Young's modulus (E_r) from 9 GPa to 9.35 GPa and from 117 GPa to 131,79 GPa, respectively. The surface roughness varied with the incorporation of W that strongly influenced the coatings' corrosion behavior. Chemical and electrochemical hydrogen charging techniques were performed to expose coated steels to hydrogen sources. W addition in the binary Al-Ti coatings strongly enhanced their resistance to hydrogen absorption. The estimated total hydrogen content trapped in the coated steel during a cathodic polarization decreased with the incorporation of W.

Keywords: *Al-Ti-W thin film, Magnetron sputtering, Hydrogen charging, Microstructure, Morphology, Mechanical properties, Chemical and Electrochemical properties.*

1. Introduction

Hydrogen represents several major challenges since the industrial revolution: economic, energetic and environmental issues due to: the enormous evolution of the annual world consumption energy for all needs (heating and cooling systems, food production...) [1], its sustainability and durability as an energy resource [2,3] and its safety for use as energy compared to the dangerous and toxic fossil fuel energy whose combustion produces carbon dioxide and deadly small particles attack the respiratory system of humans being [4,5]. Since the last decades, advanced research has been carried out in order to valorize the use of the hydrogen as an alternative energy and many studies were focused on the development of the technical feasibility of the transportation and storage of hydrogen mixtures in metallic containers such as pipelines and tanks [6,7].

The mechanisms describing the interaction of hydrogen with different metallic substrates were reported and discussed in the literature [8–11]. The diagnosis of the effects produced by the hydrogen interaction confirms the reduction of the mechanical properties [12]. This phenomenon is so-called “hydrogen embrittlement” (HE) [13–15]. The smallest chemical element penetrated into a metallic component reducing its ductility and loading capacity with two possibilities including: internal hydrogen assisted cracking (IHAC) if the damage is caused by trapped hydrogen during the material manufacturing or hydrogen pre-charging and the hydrogen environment assisted cracking (HEAC) is referred to hydrogen production and reaction with metal surfaces during mechanical loading [16–18].

Many solutions have been proposed to protect metal surfaces from hydrogen absorption and diffusion such as paint [19,20], coatings [21–23] and bulk materials doping [24,25]. Coatings are widely proposed as an efficient solution to design hydrogen barriers in order to trap the adsorbed hydrogen atoms then to avoid its diffusion towards the substrate through the interface. Oxides and ceramics represent promising candidates as hydrogen barriers such as: Al_2O_3 [26–28], Cr_2O_3 [29], Er_2O_3 [30–32], SiO_2 [33], AlN [34] and AlTiN [35], which are deposited by several techniques like chemical vapor deposition (CVD), physical vapor deposition (PVD) and sol-gel. Many studies dealt with the understanding of the hydrogen diffusion into thin films in relation with the effect of structure, microstructure [35] and interfaces [37].

The coating quality represents an important extrinsic criterion to define the hydrogen barrier efficiency. The presence of defects like porosity or cracks as well as a non-compact microstructure greatly influence the layer performance. The chemical elements constituting the protective layer should have a low permeability related to hydrogen permeation and therefore a low solubility and diffusivity [35]. Among the coatings that have these criteria, there are thin metallic glasses film, which are known by their dense morphology, smooth surface, good corrosion resistance and high mechanical properties [38]. Despite all these properties, thin film metallic glasses were not so much tested as hydrogen barriers.

In this work, new W-doped Al-Ti thin metallic films were obtained, with different chemical compositions, by magnetron co-sputtering system using three pure Al, Ti and W targets. The selection of the three chemical elements was based on many reasons: the high resistance of the bulk titanium aluminide against hydrogen embrittlement, the low permeability of hydrogen into pure titanium and tungsten materials [32] and the amorphous structure that could be obtained with these elements. Amorphous material structure is known by a homogeneous atomic distribution in the absence of any microstructural defects such as grain boundaries and dislocations; therefore of any ordinary hydrogen diffusion sites in the crystalline material such as octahedral and tetrahedral sites. Some amorphous structured coatings were recently tested and they showed promising results against hydrogen ingress and diffusion [39,40].

The first objective of this study is the deposition and characterization of new Al-Ti-W thin films with different W contents. Functional properties like corrosion properties and thermal stability were investigated. The second purpose is to examine their performance as a protective coating for steels in a hydrogen environment. The influence of W incorporation on the microstructure, amorphous state, thermal stability, mechanical properties, corrosion behavior and hydrogen permeation inhibition of the coating was discussed.

2. Experimental procedure

2.1. Elaboration Conditions

Coatings were deposited by co-sputtering magnetron system using three pure targets with 200 mm diameter. Aluminum (99.9 %), titanium (99.9 %) and tungsten (99.9 %) were powered by pulsed DC generators (frequency = 50 KHz, reverse time = 4 μ s) applying a discharge current to each target separately. The targets were located into the deposition chamber of the PVD machine (DEPHIS, France) as shown in Fig. 1, where their positions were set for all experiments to keep the same elaboration conditions. After reaching a vacuum pressure below 10^{-4} Pa, 100 sccm of argon was injected in the chamber and the film deposition was carried out at a low working pressure (0.3 Pa) and floating temperature. The distance between the target center and the substrate-holder was kept constant at 10 cm and this last one was set at 10 rpm to achieve a good atomic distribution homogeneity of the micrometric film.

2.2. Samples preparation and substrates outgazing process

Silicon wafers, glass and 100C6 steel substrates were used for the thin film deposition. They were cleaned and degreased in an ultrasonic bath of acetone, ethanol and de-ionized water progressively each for 5 min. Before cleaning process, the 100C6 steel substrates were polished and the surface roughness was measured ($R_a = 70$ nm). Table 1 gives the 100C6 steel composition.

All the 100C6 steel samples were heat treated in a vacuum furnace at a temperature of 400°C for 2 hours in order to outgas any trapped hydrogen exist in the material before the film deposition and hydrogen charging steps.

2.3. Characterization techniques

The coating microstructure and its composition were determined using a FEG Hitachi SU 8030 Scanning Electron Microscope (SEM), equipped with X-ray energy dispersive spectroscopy (EDS). The thickness of the coatings was measured by using a profilometer Altisurf 500.

Transmission electron microscopy (TEM) investigations were performed using a JEM - ARM 200F Cold FEG TEM/STEM operating at 200 kV and equipped with a spherical aberration (Cs) probe and image correctors (point resolution 0.12 nm in TEM mode and 0.078 nm in STEM mode) in order to get more precise information about the material structure,

composition and micro-structure where the analyses were carried out at the atomic scale. The TEM sample preparation was performed by the focused ion beam technique (FIB) using a FEI HELIOS Nanolab 600i.

An atomic force microscope (AFM) analysis using Veeco Bioscope II machine investigated the coating surface roughness. The thermal behavior of the thin films, containing different tungsten contents, was studied using a Setsys Evo ATG 1600 (Setaram, France). The films were deposited on molybdenum substrates to delaminate them easily without using chemical solutions. Differential Scanning Calorimeter (DSC) cycle was carried out and the glass transition and crystallization temperatures were determined using Calisto software. Small quantities of the delaminated film were put in an alumina crucible (90 μ l). The experiments were performed in Ar inert gas atmosphere with varying temperature from 25 °C to 800 °C. The heating and cooling rates were 15 k/min and 30 k/min, respectively.

The residual stresses generated in the films during the deposition procedure were calculated using the curvature method (Stoney's formula (Eq. 1)). Initially, iron substrates (50 mm x 4 mm x 0.2 mm) were thermally annealed at 450 °C for 2h in order to get a straight form relaxed from any stresses. The substrate-curvature radii before and after film deposition were measured with an optical profilometer (Altisurf 500).

$$\sigma = \frac{E_s}{6(1-\nu_s)} \frac{e_s^2}{e_f} \left(\frac{1}{R} - \frac{1}{R_0} \right) \quad (1)$$

Where E_s (181 GPa) and ν_s (0.28) are the Young's modulus and Poisson's ratio of the iron substrate, respectively. e_s and e_f are the thicknesses of the substrate and the deposited coating, respectively, while R_0 and R are the curvature radius before and after deposition, respectively.

The coating structure and phases were analyzed by X-ray diffraction using a Bruker D8 advance diffractometer equipped with a Cu-K α radiation tube ($\lambda = 0.15418$ nm), operated at 40 kV and 40 mA. Measurements were performed using coupled θ - 2θ mode. All samples were scanned from 30° to 100° and 150° 2θ diffraction angles with a scan step of 0.02° and a step time of 1 s.

The thin film mechanical properties such as reduced young modulus (E_r) and Hardness (H) were measured using Nano Indenter XP, MTS Systems equipped with a Berkovitch indenter ($E_{ind} = 1140$ GPa, $\nu_{ind} = 0.07$) and the continuous stiffness mode (CSM) option. To minimize the influence of the substrate stiffness, preliminary tests were performed for the different

samples in order to control the penetration depth (< 10 % of thin film thickness). Sixteen indents were performed for each sample and only the average values were taken into consideration. For each indent, the uncertainty was determined by the standard deviation where H and E values were interpolated from different loads, corresponding to the steady state zone of the dynamic mechanical analysis (DMA) profile that gives the adequate intrinsic values of the thin film's mechanical properties.

In a standard three-electrode electrochemical cell using Autolab PGSTAT302N potentiostat, the coating open circuit potential (ocp) was studied for 1h in NS4 solution. NS4 chemical composition is presented in Table 2. Polarization measurements in the range of -0.15 and +0.2 V/OCP at a scanning rate of 1 mV/s were performed. The extrapolation of the Tafel method was used to determine the following parameters: the corrosion current J_{corr} , the corrosion potential E_{corr} , and the polarization resistance R_p , which is described as:

$$R_p = \frac{\beta_a \cdot \beta_c}{2.303 (\beta_a + \beta_c)} \times \frac{1}{J_{corr}} \quad (2)$$

Where β_a and β_c are the inverse of the anodic and the cathodic branches slopes.

3. Hydrogen charging methods

3.1. Chemical hydrogen charging

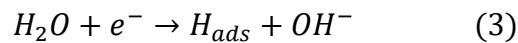
Thiocyanate ammonium solution was known as the easiest method to chemical charge samples with hydrogen [40]. Firstly, one side coated 100C6 rectangular sample with the dimensions of 4 mm×10 mm×4 mm were prepared by isolating all the other non-coated sides with Lacomit varnish. The immersion conditions applied were 20 wt.% NH_4SCN at 50 °C. After 5h of immersion in the chemical charging solution, the samples were mechanically polished with an emery paper (2400 P) and rinsed with acetone in order to prepare them for the thermal desorption analysis (TDA). A thermal desorption spectroscopy (TDS) HORIBA EMGA-621W machine was used to analyze the total hydrogen concentration into the samples by hot fusion. This desorption analysis consists in applying an induction heating of samples at a temperature of 2000 °C for few seconds, which exceeds the melting point of the steel substrate and causes the clearing of all gases contained into the coated material. The hydrogen in the sample was detected with the thermal conductivity detector (TCD). An atmosphere constituted by the argon carrier gas was heated with a given electrical power until reaching a

temperature stability. The hydrogen element leads to a modification of the environment thermal conductivity by the modification of the gas atmosphere composition.

3.2 Electrochemical hydrogen charging

The electrochemical hydrogen charging was performed using a VMP Multichannel Potentiostat. This charging was conducted in the natural soil solution NS4 (pH = 6.5). The choice of the NS4 solution was based on exposing the samples in real environment, where this composition describes the chemical state of the soil solution near pipelines [41]. This experiment aims to study the performance of Al-Ti-W coatings against hydrogen permeation during the cathodic polarization of the pipelines steel. It was performed in a standard cell containing the NS4 electrolytic solution, equipped with three electrodes: a plate platinum electrode as a counter electrode, a saturated calomel electrode (SCE) as a reference electrode and the working electrode that represents an exposed surface of 1 cm² as shown in figure 2. The distance between the counter electrode and the working electrode was 20 mm. The applied cathodic current was fixed after studying the cathodic polarization of the 100C6 substrate and the different Al-Ti-(W) thin films in the NS4 solution.

During the electrochemical charging process, the adsorbed hydrogen atoms, generated on the coated and uncoated 100C6 steel surfaces, were obtained from the reduction of water molecules, which is expressed by the following reaction:



The total hydrogen quantity produced was deduced from the monitoring of the cathodic current evolution along the exposition time, which is defined as:

$$QH_{generated} = \int_0^{tch} I_{cath} dt ; E_{cath} = constant \quad (4)$$

For the determination of the trapped hydrogen concentration in the 100C6 steel, a discharging process was performed. However, just after hydrogen charging in NS4 solution, the samples were immediately rinsed with 0.2M NaOH solution (pH = 12.4) and then transformed to another double electrochemical cell. The first half-cell contains an electrolytic solution of 0.2M NaOH in which is immersed a plate platinum auxiliary electrode. The second half-cell

is filled with a KCl solution in the presence of the calomel-saturated electrode. Both cells were linked by a salt bridge.

The hydrogen effusion from the sample immersed in NaOH solution was carried out under an anodic polarization by controlling the anodic potential, which was fixed at +0.168 V/SCE that represents the potential of passivation zone in order to avoid the surface oxidation. The registering of the anodic current was performed as a function of time.

In order to study the impact of various exposure times and the difference between steel substrate and coating composition and nature against the hydrogen absorption, the discharge time (t_{dis}) was fixed for 30 min and the quantity of hydrogen already existed in the material before the charging process was measured. The quantity of hydrogen absorbed after hydrogen charging can be defined as:

$$QH\ abs = \int_0^{t_{dis}} [I_{an}(t) - I_{an.ref}(t)] dt ; E_{an} = constant \quad (5)$$

Where $I_{an}(t)$ corresponds to the anodic polarization current of the hydrogen charged 100C6 steel samples and $I_{an.ref}(t)$ corresponds to the oxidation current of the samples without hydrogen charging in order to determinate the quantity of hydrogen already present in the sample. The hydrogen concentration (C_H) was determined using the following equation:

$$C_H = \frac{QH\ abs}{n * F * V} \quad (6)$$

V is the effective volume of the sample, n is the number of the electrons lost according to the anodic reaction, which is 1 in our case: $H_{abs} \longrightarrow H^+ + e^-$; and F is the Faraday constant. The efficiency of the hydrogen permeation through the steel surface could be explained by the efficiency coefficient (K), which is defined as:

$$K = \frac{Q_{abs}}{Q_{generated}} \quad (7)$$

The performance of coatings against the hydrogen ingress after any type of loading is deduced from the reduction factor R , which is defined as:

$$R (\%) = \frac{CH\ bare.\ substrate - CH_{coated.\ substrate}}{CH\ bare.\ substrate} \times 100 \quad (8)$$

The reduction factor R is expected to be very high for the coated 100C6 compared to the uncoated one. An improvement of the performance of the coating against hydrogen diffusion is desirable by the incorporating of W element in order to reach a reduction factor of 100%, thus achieving our goal, which is the protection of the bulk material against HE by developing of hydrogen barrier coating as the true meaning of the word.

4. Results

4.1. Chemical composition of Al-Ti-W thin films

In addition to the deposition conditions of Al-Ti-(W) coatings described in section 2.1, the substrate-holder polarization was necessary to enhance the adherence onto steel substrate. A polarization of 30 V was applied to the substrate-holder by using a bias generator for the first 5 min of film deposition. The targets were pre-sputtered for 10 min to remove the oxides and other contaminants. The optimal deposition parameters of Al-Ti-W thin films are presented in table 3. The W content and composition ratio of $W/(W+Ti+Al)$ increased from 0 to 17.5 at% and 0 to 0.17, respectively, as the W target current increased from 0 A to 0.8 A. The Ti and Al chemical composition decreased gradually from 45.7 at % to 37.5 at % and from 54.3 at% to 45 at%, respectively as listed in table 3. After measuring the deposition rate, the deposition time was adapted to obtain an average thickness of 4 μm for all coatings.

The chemical compositions of different films were measured by EDX technique applying 20 kV accelerating voltage. The results showed the presence of the basic elements constituting the coatings. The Ti/Al ratio of about 0.8 was respected in the different coatings and the peaks of contamination elements such as oxygen and carbon were nonexistent, which is helpful for focusing only on the investigation of the W addition effects. The incorporation of W was confirmed by the appearance of its peaks in the EDX spectra. The elemental mappings at different scales and zones confirm the coating homogeneity in term of elements distribution as for all Al-Ti-(W) coatings composition.

4.2. Morphology and surface topography of Al-Ti-W thin films

Fig. 4 shows the cross-section SEM images of Al-Ti-(W) coatings. A typical dense, cracks free microstructure was observed and an average of 4 μm uniform coating thickness in different samples and zones was confirmed. The increasing of the deposition rate from 1.35

$\mu\text{m.h}^{-1}$ to $1.75 \mu\text{m.h}^{-1}$ corresponds respectively to the amorphous Al-Ti and the Ti-Al-17% W (table 3). This increase in deposition rate is due to the increase of pulsed direct current applied to the W target from 0 A to 0.8 A.

Fig. 5 shows cross-section TEM images of $\text{Al}_{45}\text{Ti}_{38}\text{W}_{17}$ thin film. The bright field (BFTEM) (Fig. 5 a) confirms the non-columnar film growth from the substrate surface as well as the good adhesion between the 100C6 steel and the micrometric film. Fig. 5 b presents a high resolution TEM image of the same thin film composition accompanied by a selected area electron diffraction (SAED) pattern. A typical halo SAED pattern of thin film metallic glasses was obtained indicating the amorphous structure of the as-deposited $\text{Al}_{45}\text{Ti}_{38}\text{W}_{17}$ film.

Fig. 6 illustrates the AFM surface topography of each coating obtained from scanning $4 \mu\text{m}^2$ areas. The average surface roughness (RMS) was calculated from 3 different locations and determined using Gwydion software. This figure shows very smooth surfaces, where roughness is in the range of 1.09 to 3.12 nm with different W incorporation amount. The SEM images and DRX analysis confirm the coatings surface roughness state due to the absence of columnar microstructure during the film growth as well as the absence of the grain boundaries that defines the amorphous nature of the Al-Ti-(W) thin films. The W incorporation led to a slight increase of the surface roughness where it reached its highest value with 11% W amount that could be explained by the highest compressive intrinsic stress created during deposition step of this thin film. The Al-Ti-(W) thin films surface roughness looks similar to other thin films such as Zr based metallic glass thin films [43,44] and $\text{Fe}_{44}\text{Cr}_{15}\text{Mo}_{14}\text{Co}_7\text{C}_{10}\text{B}_5\text{Si}_5$ thin film metallic glass [45].

4.3. Amorphous state analysis

According to Inoue et al. [46], there are three main conditions that are able to form a bulk metallic glass, which are:

- 1) more than three elements constituting the material,
- 2) a significant atomic mismatches above 12% among the main elements, and
- 3) negative heat of mixing among the main elements.

The atomic radii of the three elements and the difference between each atoms pair were listed in table 4. It is obvious that the differences of atomic radii percentages, which were calculated using the following method, are not enough important.

$$\text{The differences of atomic radii of A and B elements (\%)} = \frac{Ra-Rb}{Rb} \times 100 \quad (9)$$

The maximum difference between two atomic radii is obtained for W-Ti atoms pair which is < 8%. So the differences of atomic radii of the Al,Ti and W elements are not the driving force for the amorphous structure because it cannot fulfill the Inoue second criteria. On the other hand, the heats of mixing of atomic pairs [47] of Al, Ti, and W elements [48] are listed in table 5 where W-Ti, W-Al and Ti-Al pairs have all negative heats of mixing, encouraged the amorphous structure formation when these elements are mixed.

Although only one of the mentioned three conditions was achieved, the binary Al-Ti film and the new Al-Ti-W films are metallic glass. It seems that, in our system composed of three elements, the heat of mixing represents the main criteria that favors the amorphous state. The amorphous state of the Al-Ti thin films elaborated by magnetron sputtering process was observed by A. Billard et al. [48] who studied and classified the Al-Ti structure as a function of the aluminum content. The same results were confirmed by F. Sanchette et al. [49] when they characterized the Al-Ti thin film with the Al/Ti ratio of 1.27 that had a similar trend to those studied in this work.

XRD patterns of the Al-Ti films containing different tungsten concentrations are presented in figure 7. All those patterns present the same behavior. A broad peak was obtained in the 2θ range from 34° to 45° , which presents the classical amorphous phase of thin film and bulk metallic glasses. These results are very consistent with those obtained from the SAED pattern analysed by the TEM technique. The broadening of peaks is generally used for the calculation of the distance between the nearest neighbor atoms using the following Ehrenfest formula [50].

$$d = \frac{0.615 * \lambda}{\sin\theta} \quad (10)$$

Here λ and θ are the X-ray wavelength and the scattering broad peak angle, respectively.

The amorphous hump position shows a slight shift towards higher diffraction angles with different W amount incorporation, which indicates an evolution of the closest neighbors' atoms inside the amorphous matrix. The distance between the closest neighbors showed a slight variation, a decrease from a value of 2.85 \AA for the W-free Al-Ti to 2.79 \AA with 17% at of incorporated W element as listed in the following table 7.

4.4. Thermal behavior of Al-Ti-W thin films

Fig. 8 illustrates the DSC spectra of four coatings containing different W concentrations. The glass transition temperature T_g , the starting crystallization temperature T_x , the crystallization temperature peak T_p and ΔT presenting the difference between the T_x and T_g (it defines the supercooled liquid region), were extrapolated from exothermic peaks of DSC curves and listed in table 7. The increase of tungsten content in the coating from 0 to 17 at% led to increase the T_g , T_x and T_p from 423 °C, 466 °C and 490 °C, respectively, to 556 °C, 600 °C and (637/690)° C, whereas the variation of ΔT is random and independent of tungsten content. The highest and lowest ΔT values of 44 °C and 27 °C correspond to films containing 11 and 4 at% of W, respectively. However, the ΔT value of W-free film is 43 °C. The shift of the exothermic peaks to a higher temperature with the incorporation of W element can be explained by the increase of the thin films' heat activation energy. This phenomenon was observed by C.H. Lin et al [50] who studied the addition of 2.3 at % insoluble W element in the amorphous pure copper thin film. The W addition resulted a raising of temperature of crystalline phases formation. The DSC curve of film with 11 at % of W showed two exothermic peaks. This could be explained by the formation of more than one crystalline phase. A similar curve shape was shown in the study of Ni-P-(W) coating [51]. At high heating rate, addition of W element increased the number of exothermic peaks that was explained by the crystallization of intermediate phases and the formation of stable crystal phases.

4.5. Phase stability and microstructure analysis after heat treatment

Figs. 9, 10 and 11 show the XRD patterns of $Al_{54}Ti_{46}$, $Al_{49}Ti_{40}W_{11}$ and $Al_{45}Ti_{38}W_{17}$ thin films obtained after heat treatment at various temperatures. The structure stability of the coatings was noticed from the DSC analysis as mentioned in the previous section then it was confirmed with an annealing treatment in vacuum. The as-deposited $Al_{54}Ti_{46}$ coating had a non-crystalline amorphous structure characterized by a broad peak. At 500 °C, a tetragonal intermetallic γ -AlTi phase appeared (according to the international center for diffraction data (ICDD) PDF 03-065-5414 database) and the amorphous structure was transformed to crystalline one.

For comparison, the crystallization temperature values of $\text{Al}_{63}\text{Ti}_{37}$ and $\text{Ti}_{53}\text{Al}_{47}$ reported in the literature were 600 °C and 400 °C, respectively, which the XRD peaks of the crystalline coatings indicated the existence of $\gamma\text{-Al-Ti}$ and $\alpha_2\text{TiAl}_3$ phases [52,53]. These results are close to those of $\text{Al}_{54}\text{Ti}_{46}$ coating studied in this work.

The incorporation of 11 at% of W led to the formation of a second phase. The crystalline structure took place at an annealing temperature of 650°C as shown in the Fig. 10 with the presence of two phases: $\gamma\text{-Al-Ti}$ and a new bcc β TiW phase according to the ICDD PDF 03-065-6898 database. This result confirms the DSC analysis and explains the overlapped two exothermic peaks shown in previous section for the film containing 11 at % of W. The thermal stability of the amorphous film containing 17 at% of W reached 550 °C and the coating crystallization was noticed after an annealing at 650 °C presenting only the appearance of a Bcc β TiW phase. This phenomenon was obtained by Hashimoto et al [53] who studied the ternary bulk AlTi-(W) alloy at high temperature and concluded that W acts as the strongest β phase stabilizer when its content exceeds 1 at% in the Al-Ti-W system. For thin films, It is obvious that the addition of 17 at% of W element stabilizes the β TiW phase starting from 650 °C.

4.6. Mechanical proprieties and residual stress measurements

Table 8 illustrates the evolution of mechanical properties (hardness and Young's modulus) and residual stress generated in the Al-Ti-(W) thin films during the deposition process.

The intrinsic stress value in the pure amorphous Al-Ti was 44 MPa indicating a tensile stress, which is close to the intrinsic stress nature studied after doping Aluminum with 15 at% of titanium element [49]. The intrinsic stress nature was changed after the addition of W element to AlTi film. We can notice from table table 8 that all W-depod AlTi films had compressive stresses and the highest value of -24 MPa was found in the film containing 11 at % of W. According to the literature, the most studied amorphous thin films showed a compressive intrinsic behavior which increases as the molar mass of the alloy increases [55] so with the addition of W element, the molar mass of the AlTi-(W) increases as well as the compressive intrinsic stress. The same behavior was reported by Wang et al [55] who studied the incorporation of W in the diamond like carbon amorphous films.

It is obvious also that the values of the residual stresses are low whatever its nature. This could be explained by the absence of thermal stress where the coatings were elaborated at low

temperature using magnetron sputtering process in addition to the absence of structural stress generated by crystallinity defects (grain boundaries, dislocations...). It could be also due to the heterogeneous repartition of residual stress along the film thickness related to the curvature method used for calculation the average film stress (Macroscopic study). The transition from a tensile to a compressive stress with W doping could be also explained by the increase of film compactness; knowing that this phenomenon still a controversial issue [56].

The evolutions of hardness H , Young's modulus E_r , and H/E_r ratio of Al-Ti-(W) films containing different incorporated W amounts are shown in figure 12 and table 8. The hardness of different AlTi-(W) thin films was practically constant. It indicates a very slight variation where the minimum hardness was 8.59 GPa for the film with 11 at% of W and the maximum hardness of 9.35 GPa was found for the film containing the highest W amount (17 at%). Young's modulus increased from 117 to 132 GPa with the increase of W content in the deposited films. The same behavior was obtained for the W-incorporated Zr-Ti thin film metallic glass [57]. In the amorphous thin films, the mechanical properties essentially depend on the film composition and the material density, which is generally linked to the cohesion energy of the atoms constituting the material. The increase of W content reduced the interatomic distance between the closest neighbors' atoms as listed in table 6, which led to a denser atomic packing state. This late one justifies the increase of film hardness and Young's modulus. The hardness and Young's modulus of the material are very sensitive to the quality of the deposited films including the porosity, voids and roughness. This phenomenon was noticed for the thin film containing 11 at% of W where its morphology affected these mechanical properties. The H/E_r ratio decreased from 0.077 to 0.068 with the addition of tungsten indicating a decrease in the elastic resistance of the glass metallic thin films.

Compared to the literatures, the hardness and elasticity modulus of the AlTi-(W) amorphous thin films studied in this work are higher than the Al-W [58], and Zr-W-Ti [57] thin films values and similar to the Fe-Zr-Ti [59] film properties.

4.7. Corrosion behavior of the AlTi-(W) coatings in NS4 solution

The evolution of open circuit potential (OCP) for the ternary coatings is shown in figure 13. Without a tungsten element, the $Al_{54}Ti_{46}$ thin film showed a fast stability in corrosion potential curve during the immersion time with a value of -0.53 V/SCE. The OCP was strongly shifted toward more cathodic value with the addition of 4 at% of W. An initial OCP value was close to -0.98 V/SCE and gradually increased during the immersion. Similar OCP

evolution was observed for the film containing 11 at% of W during the immersion whereas the film containing 17 at% of W had a quasi constant OCP value around -0.83 V/SCE. The peculiar behavior of OCP evolution of 4 at% of W and 11 at% of W was related to the slight variation of Ti/Al ratio with a values of 0.89 and 0.80, respectively that lead to increase of Al and Ti elements in the films compared to the two other film compositions and to evolution of its OCP curves to more anodic values.

Figure 14 presents the polarization curves of the thin films after 1h of immersion in NS4 solution. The electrochemical parameters deduced from the polarization curves are gathered in Table 9.

The binary Al-Ti alloy presented the highest value of corrosion potential and the lowest corrosion current density. The corrosion potential was close to -0.53 V/SCE, in good agreement with the open circuit potential obtained in figure 13. The highest corrosion resistance was obtained for the $\text{Al}_{54}\text{Ti}_{46}$ film with a value of $954 \text{ K}\Omega\cdot\text{cm}^2$, corresponding to the lowest current density of 54 nA/cm^2 . The slope of the anodic branch, corresponding to the oxydation mechanism, suggests a rapid passivation of the film, resulting in a very low anodic current density in a large range of anodic potential [60,61].

Incorporation of W led to the shift of corrosion potential towards more negative values and also the increase of reactivity in NS4 solution. A significant decrease in the anticorrosion performance of the binary Al-Ti alloy was noted by the addition of W. Similar conclusions were also reported during the corrosion studies in a saline solution of alloys deposited by magnetron sputtering, W-Cu alloys fabricated by powder metallurgy in neutral (pH= 7) NaCl solution [62] and Ni-W elaborated by an electrodeposition method [63].

For the Al-Ti film with 4 at% of W, the corrosion potential was estimated at -0,76 V/SCE suggesting that the incorporation of tungsten affected and delayed the passive behavior of Al and Ti. The anodic polarization curve presented a quite increase in the current density suggesting a higher reactivity. Then, the anodic current density reached a quite constant value at around 260 nA/cm^2 that could be explained by the formation of protective corrosion products due to the presence of alloying elements with a strong passivation ability such as Al and Ti [64]. For the film with 11 at.% of W, a quite singular behavior was observed with a polarisation curve quite similar to that of the film with 4 at.% W. Its corrosion potential value was estimated at -0,69 V/SCE and the highest corrosion current was 580 nA/cm^2 , which corresponds to corrosion resistance of $98.60 \text{ k}\Omega\cdot\text{cm}^2$. This peculiar behavior is probably linked to the increase of the film surface roughness to 3.12 nm that favors the film reactivity

with the active particles of the electrolyte solution. For the film with 17 at.% of W, the corrosion potential was -0,83 V/SCE, the corrosion current density was 162 nA/cm² and the R was 147.11 kΩ.cm² confirming that W incorporation delays and modifies the passive behavior of the Al-Ti alloy.

The incorporation of W element in the Al-Ti amorphous thin film, whatever its concentration, impacted its corrosion resistance. Many studies indicate that W incorporation increases the film activity and is probably incorporated in the composition of the AlTi passive film, which explains the less protective character of Al-Ti-(W) films [65,66].

7.8. Al-Ti-(W) thin film behavior under hydrogen Chemical charging

Hydrogen chemical charging during 5h in an ammonium thiocyanate solution was performed for all samples. After the chemical charging step, the samples were rinsed with acetone, then immediately tested in order to avoid the effusion of hydrogen and measure the absorbed quantity in the material. The hydrogen charging and TDS analysis were carried out four times for each sample where only the hydrogen concentration average was considered and illustrated in table 10.

Hot extraction spectra of the coatings are presented in figure 15 and describe the evolution of the hydrogen release versus time. The different spectra present a peak whose area defines the concentration of hydrogen absorbed in the material during the chemical charging. As shown in figure 15, the maximum of the peak decreased with the W content. For an exposed area of 40 mm², the hydrogen concentration C_H was calculated. Figure 16 presents the evolution of the total hydrogen content and reduction factor versus the W incorporation. The maximum value of 5.2 wppm was found for the bare steel sample (reference sample). Al-Ti-(W) thin films played an important role in the protection of steel against hydrogen ingress. The hydrogen concentration was 2.5 wppm in coated steel with an amorphous Al₅₄Ti₄₆ film. Addition of W led to enhance its performance and the best protective film was obtained for the film containing 17 at% of tungsten (C_H = 1.66 ppm). The absorbed hydrogen amount in the coated steel sample was reduced to 69% compared to the hydrogen concentration absorbed in the uncoated steel sample. SEM images analyses of the AlTi-(W) thin films deposited on Si wafers were carried out after 5h hydrogen charging in the thiocyanate solution. A nanometric oxide film was detected as shown in figure 17 as a result of corrosion products during the charging process [40], which explains the high reduction factor obtained with this charging method. Certainly the oxide films of aluminium, titanium and tungsten

played an important role as a first hydrogen barrier that block its diffusion. The oxides forming from these three chemical elements are known with their high permeation reduction factor (PRF) against hydrogen permeation [35].

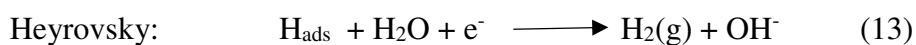
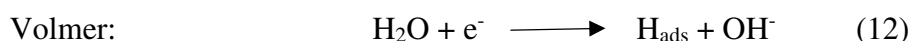
7.9. Al-Ti-(W) thin film behavior under hydrogen electrochemical charging in NS4 solution

During chemical charging, the coating surface is able to react with the corrosion products and influences the hydrogen ingress. In order to study only the performance of the coatings and the influence of W incorporated in the thin film, a second experiment was performed using electrochemical charging in NS4 solution at a cathodic potential of -2 V/SCE. At this potential value, the main reaction that occurs on the coated samples is the hydrogen evolution reaction (HER) [67]. This was concluded after studying the cathodic polarization behavior of the bare 100C6 steel and the coated ones with Al-Ti, Al-Ti-W (11 at%), and Al-Ti-W (17 at%) in a NS4 electrolyte solution as shown in figure 18. The polarization curves present the current density as a function of the applied cathodic potential. For all tested samples, we can see that the curves can be divided into three zones: I, II and III. These zones describe the different types of reactions that took place with varying the applied cathodic potential.

Zones I and II are dominated and driven by the dissolved oxygen reduction reaction (ORR) limited by electron and diffusion transfer, respectively:



Zone III is dominated and driven by the hydrogen evolution reactions (HER):



In order to avoid the reactions dominated by oxygen reduction which can disturb the production as well as the adsorption of hydrogen on the samples surfaces, the choice of -2 V/SCE applied potential was registered in zone III as mentioned in figure 18.

Table 11 illustrates the cathodic current values (I_{cathodic}), hydrogen charging exposure time (T_{charg}), hydrogen quantity already exist in the sample before charging $Q_{\text{an.ref}}$, the calculated quantity of created hydrogen (Q_{created}), the quantity of absorbed hydrogen (Q_{absorbed}), the

hydrogen concentration (C_H) and hydrogen absorption efficiency coefficient (K) using the following equations:

$$QH_{generated} = \int_0^{t_{ch}} I_{cath} dt ; E_{cath} = -2 V/SCE \quad (4 *)$$

$$QH_{abs} = \int_0^{t_{dis}} [I_{an}(t) - I_{an.ref}(t)] dt ; E_{an} = +0.168 V/SCE \quad (5 *)$$

$$C_H = \frac{QH_{abs}}{n * F * V} \quad (6 *)$$

$$K = \frac{Q_{abs}}{Q_{generated}} \quad (7 *)$$

Figure 19 (a, b and c) describes the variation of $Q_{created}$, C_H , and K coefficients as a function of hydrogen exposure time, respectively. The performance of different samples under hydrogen electrochemical charging was investigated for three times 30, 60 and 300 min.

Figure 19 (a) shows the variation of hydrogen quantity generated on the surface of the working electrode (sample) by an electrochemical exchange in the NS4 electrolyte. This later one resulted the circulation of an electric cathodic current that led to the production of hydrogen as mentioned in the previous paragraph. A linear increase of $Q_{generated}$ as a function of exposure time was noticed for the bare steel surface. A similar trend was shown for the thin films surfaces with hydrogen created quantities less important compared to the bare steel at various exposure times. At the first 30 min of electrochemical charging, the difference between the created hydrogen quantities for all samples was minimal. The highest value was 8300.3 mA.s for the bare steel. There was no a significant difference between the values obtained for the thin films. They presented close values of 3599.97 mA.s, 3657.9 mA.s and 3545.9 mA.s corresponding to Al-Ti, Al-Ti-(11 at% W) and Al-Ti-(17 at% W), respectively. After 60 min of hydrogen charging, the difference between the linear curves becomes larger where the $Q_{generated}$ for the different samples increased. The highest $Q_{generated}$ value of 100783 mA.s was also found for the uncoated 100C6 steel, which corresponds to a cathodic current density of 5 mA/Cm². The lower $Q_{generated}$ values of 7869.36 mA.s, 7817 mA.s and 13214 mA.s correspond to the cathodic current densities of 2.2 mA/Cm², 1.8 mA/Cm² and 4.3 mA/Cm² for Al-Ti, Al-Ti-(11 at% W) and Al-Ti-(17 at% W), respectively. For 5 h of hydrogen charging, we notice that the $Q_{generated}$ on the film containing 17 at.% of W

was close to that produced on the bare steel sample. Its value of 82456.4 mA.s corresponds to a 5.1 mA/Cm² current density. The $Q_{\text{generated}}$ on Al-Ti, Al-Ti-(11 at% W) and bare steel were 44939.7 mA.s, 50547 mA.s and 100783 mA.s corresponding to 2.5 mA/Cm², 3.5 mA/Cm² and 5.7 mA/Cm², respectively.

The results shown in figure 19 (a) are very compatible with those in figure 17 where the cathodic polarization curves showed the same behavior of surface conductivity for the different surfaces whatever the applied cathodic potential. Referred to figures 19 (a) and 18, we can conclude that the incorporation of W element in Al-Ti amorphous thin film led to increase its electric conductivity, which still lower than that of the bare steel surface. The results shown in figure 19 (a) could be also explained by the ability of W element to reactivate the sample surfaces containing passive films called “native oxides”. The passive films constituted from aluminium and titanium elements can limit the cathodic reactions by slowing down the electronic exchange on the sample surface. The corrosion study of the AlTi-(W) thin films showed that the addition of W element decreased its corrosion resistance by destabilising the passive film and reactivating the thin film surface.

Figure 19(b) shows the variation of absorbed hydrogen concentration (C_H) in the bare 100C6 steel and the AlTi-(W) thin films as a function of hydrogen charging exposition time. The hydrogen concentration was calculated using eq (6*) after determining the Q_{abs} , which corresponds to the quantity of hydrogen absorbed during the discharging process in the NaOH solution (0.1M). This valorizes the hydrogen effusion from the steel samples, that was calculated using eq (5*). The quantities of hydrogen already existing in the samples ($Q_{\text{an.ref}}$) without being subjected to a hydrogen charging was calculated and listed in table 11. The concentration of absorbed hydrogen in the bare steel was higher than that in the coated samples. At 30, 60 and 300 min exposure time, the hydrogen concentrations were $1.640 \cdot 10^{-6}$ mol/cm³, $1.045 \cdot 10^{-6}$ mol/cm³ and $2.136 \cdot 10^{-6}$ mol/cm³, respectively. The coated steel with Al-Ti amorphous thin film showed a decrease in the absorbed hydrogen concentration to $0.498 \cdot 10^{-6}$ mol/cm³, $0.603 \cdot 10^{-6}$ mol/cm³ and $1.936 \cdot 10^{-6}$ mol/cm³ with increasing the hydrogen charging time. The addition of 17 at% of W element to the Al-Ti thin film reduced more the concentration of the absorbed hydrogen to reach $0.361 \cdot 10^{-6}$ mol/cm³, $0.303 \cdot 10^{-6}$ mol/cm³ and $1.844 \cdot 10^{-6}$ mol/cm³ after 30, 60 and 300 min charging time, respectively. As mentioned in the majority of previous analyses, the amorphous Al-Ti thin film with 11 at% of W showed a particular behavior even in hydrogen electrochemical charging. After 30 min hydrogen charging, the C_H value in the coated steel with AlTi-(11 at% W) was $0.855 \cdot 10^{-6}$

mol/cm³, which is higher than that of AlTi film. This particularity disappeared at 60 min and 300 min charging time where the C_H values were 0.574.10⁻⁶ mol/cm³ and 1.871.10⁻⁶ mol/cm³, respectively. These values are lower than the C_H ones in the AlTi-coated steel. It showed the same trend as the W incorporation influences the absorbed hydrogen concentration in thin films (as shown in Al-Ti film containing 17 at% W). This individuality is also noticed in figure 19 (b) for the same exposition time (30 min) where the generated hydrogen quantity on AlTi-(11 at% W) surface was slightly higher than that of AlTi-(17 at% W). This singularity could be explained by the difference of thin film surface topographies where the AFM analysis showed that the surface roughness of AlTi-(11 at% W) thin film was twice higher than the AlTi and AlTi-(17 at% W) roughness. So for a fixed exposed surface to hydrogen (1 cm²), the more the roughness is important, the more hydrogen evolution reactions take place. Therefore more hydrogen adsorbed sites are created and higher the absorbed hydrogen concentration is produced.

The hydrogen absorption efficiency coefficient (K), which describes the exposition state of the working electrode surfaces (samples) against hydrogen ingress, is presented in figure 19 (c). This parameter, which was calculated using eq (7*), confirmed the results shown in figure 19 (a and b). Whatever the exposition time, the K coefficient was very low for the film containing 17 at% of W with 3.94. 10⁻³, 0.88. 10⁻³, 0.86. 10⁻³ values. However, it was higher for W-free coated surfaces, which indicates a strict hydrogen exposition state with 5.34. 10⁻³, 2.96. 10⁻³, and 1.66. 10⁻³ values corresponding to 30 min, 60 min and 300 min of hydrogen charging exposition time, respectively. The highest K value was 9.02. 10⁻³ corresponding to the film containing 17 at% of W after 30 min of charging indicating a very strict exposition due to its surface topography as explained in the previous paragraph.

Figure 20 shows the decrease of hydrogen reduction factor R as a function of W content in the AlTi-(W) amorphous thin films for various hydrogen charging times (30 min, 60 min and 300 min). The highest reduction factor was 69.7% corresponding to the film containing 17 at% of W after 30 min of charging and the lowest R (9.36%) was obtained for the Al₅₄Ti₄₆ film after 5h hydrogen charging. For all coatings, the R factor was dramatically decreased with increasing the hydrogen charging time. For the Al₄₅Ti₃₈W₁₇ film, R decreased from 69.7% to 15.83%.

5. Discussion

Metallurgical defects in metallic materials such as grain boundaries, dislocations, inclusions and precipitates affect hydrogen permeation by creating fragile zones in the material that are responsible for cracks initiation [68,69]. Amorphous coatings were developed and deposited on 100C6 steel samples for testing as hydrogen barriers.

The coating based on the two basic elements, Al and Ti, represented an amorphous structure with an atomic composition of 54.4 at% and 45.6 at%, respectively. With this composition, the coating showed a dense morphology as shown in figures 4 and 5, a smooth surface roughness and an excellent corrosion behavior in NS4 solution with a corrosion resistance of 954 kΩ.cm² and a -0,53 V/SCE corrosion potential. The Al-Ti binary coatings reduced the hydrogen concentration by 50 % with hydrogen chemical charging and 9% with electrochemical cathodic polarization.

The addition of tungsten to the Ti₄₆Al₅₄ film did not cause any changes in film structure and its state remained amorphous with a W concentration ≤ 17 at %. Doping the Al-Ti film with W led to increase its densification and compactness by the reduction of interatomic distance between its closest neighbors atoms from 2.85 Å to 2.79 Å that results the increase of the thin film hardness (H) and reduced elasticity modulus (Er). The film compactness was also explained by the evaluation of residual stress generated during the coating elaboration where a transition behavior from tensile to compressive residual stress was shown. Increasing the micrometric film compactness caused a slight increase in surface roughness to reach its highest value (3.12 nm) with the incorporation of 11 at% W. Therefore, more surface defects and free energy surfaces explain the reduction of corrosion behavior of W-doped coatings as well as the W element intrinsic criteria that is less noble than Al and Ti elements acting as a passive film destabilizer. Coatings containing W valorize the thermal stability of the amorphous structure. The crystallization temperature (Tx) was increased with the addition of 17 at% W from 466°C to 630°C due to the increase of the heat activation energy of the thin film. Thermal stability was confirmed by a vacuum heat treatment of the thin films containing different W concentrations. The crystallization of the free-W thin film was achieved at 500°C by the appearance of tetragonal intermetallic γ-Al-Ti phase. The W incorporation led to the stabilization of β TiW phase where aluminium was found in solid solution of the bcc β TiW structure at a temperature of 650°C (for the film containing 17 at % W).

The increase of W concentration in coating enhanced its resistance behavior against hydrogen diffusion. This is not only because of the micro-porosity density reduction by the increase of the coating micro-structure compactness as explained in the previous paragraph, but also with

its ability as a chemical element to decrease the amount of diffusible hydrogen in the coated 100C6 steel. This was proved with the TDS test as shown in figure 15 under the same hydrogen charging conditions.

Figure 19 shows that despite the increase of the quantity of hydrogen generated on the sample surface with the increase of W amount in the thin film, the absorbed hydrogen concentration decreased. This confirms that even W element increases the sample surface activity by destabilizing the passive films “native oxides” covering the sample surface, it is still complicated for hydrogen to permeate through a film containing W.

Fig. 20 shows the influence of W addition on the coating performance by the increase of R factor compared to the W-free coating. For different exposition times, thin film containing 17 at% W ($\text{Al}_{45}\text{Ti}_{38}\text{W}_{17}$ film) represented the best composition against hydrogen ingress. This indicates that more W concentration in the coating is, more the hydrogen diffusion into the coating would be difficult.

The reduction ability of tungsten against hydrogen was decreased with increasing the exposition time to reach 15 % after 5h of hydrogen charging in a cathodic polarization, whereas the R factor of the same coating composition was 69 % under chemical charging. The large difference between the R-values for the both hydrogen charging is shown in Fig. 21. This is explained by the formation of oxide film caused by the corrosion reactions during the chemical charging in the thiocyanate ammonium solution [41] as shown in Fig. 17. The oxide film constituted from Al, Ti and W elements played the role of the first hydrogen barrier, where the hydrogen diffusivity was significantly decreased.

6. Conclusion

In this paper, a new Al-Ti-W metallic glass thin film was developed. Many films were deposited by a magnetron co-sputtering system on Si wafer, glass and 100C6 steel substrates. The structure, microstructure, thermal stability, surface topography and mechanical properties of the coatings with different tungsten concentrations were investigated. The corrosion behavior of the coatings in a NS4 solution was studied and the influence of W addition on the performance of the films against hydrogen diffusion with preliminary tests was discussed. The following statements draw the main conclusions of this study:

- 1) A dense morphology of 4 μm thin film and smooth surfaces, which did not exceed 4 nm roughness, were obtained for all films with different W contents.
- 2) A nano-crystalline amorphous structure was obtained for all Al-Ti-(W) films. The TEM observations confirmed the amorphous state of films containing ≤ 17 at% of W. DCS analyses confirmed that the addition of W results in an increase of crystallization temperature. It was increased from 466° to 630°C after doping Al-Ti thin film with 17 at% W.
- 3) Thermal stability of the amorphous structure was confirmed with a heat treatment in a vacuum furnace for $\text{Al}_{54}\text{Ti}_{46}$, $\text{Al}_{49}\text{Ti}_{40}\text{W}_{11}$ and $\text{Al}_{45}\text{Ti}_{38}\text{W}_{17}$. The appearance of crystalline structures of three films were obtained at 466 °C, 600 °C and 630 °C with the appearance of the tetragonal γ Al-Ti, γ Al-Ti and βTiW phases, and only βTiW phase, respectively.
- 4) The thin film hardness (H) and the reduced Young's modulus (E_r) increased with the increase of W content from 9.05 GPa to 9.35 GPa and from 117 GPa to 132 GPa for $\text{Al}_{54}\text{Ti}_{46}$ and $\text{Al}_{45}\text{Ti}_{38}\text{W}_{17}$ thin films, respectively.
- 5) The excellent corrosion resistance of the $\text{Al}_{54}\text{Ti}_{46}$ film in a NS4 solution (954 $\text{K}\Omega\cdot\text{cm}^2$) was reduced to 98.60 $\text{K}\Omega\cdot\text{cm}^2$ with the W addition and the increase of coating surface roughness.
- 6) The coatings' structures and thicknesses were kept constant and preliminary tests on hydrogen permeation were carried out and discussed. The influence of amorphous $\text{Al}_{54}\text{Ti}_{46}$ and W addition were investigated.
- 7) After hydrogen chemical charging, it has been found that the quantity of hydrogen absorbed was decreased with the increase of W content in the coatings. The R factor reached 69.7% for the film containing 17 at % of W after 5h exposure time. The high value of R factor was due to the oxide film formed during the hydrogen chemical charging, which is due to the redox reactions produced on the sample surface. This oxide layer played the first hydrogen barrier.
- 8) The electrochemical hydrogen charging allowed to calculate the hydrogen concentration after different exposition times (30 min, 60 min, and 300 min). The W addition induced an increase in the hydrogen desorption activation energy in a cathodic polarization with an R factor reaching 15%.
- 9) The results obtained from the both hydrogen charging methods confirm that the $\text{Al}_{45}\text{Ti}_{38}\text{W}_{17}$ thin film presents the best hydrogen barrier performance.

Acknowledgment

The authors would like to thank Mr. Régis Deturche, Engineer at the UTT, for his help in performing AFM tests and Mr. Cyril Berziou, Technician at LaSIE, for his assistance in hydrogen chemical charging.

The authors would like to thank the European Union (FEDER - Fond Européen de Développement Régional), co-funder of DERBHY project, and also the GIP52 (Groupement d'Interet Public Haute-Marne) for their financial support.

References

- [1] *Bp Statistical Review of World Energy 2020*, 68 (2020).
- [2] B. Pivovar, N. Rustagi, and S. Satyapal, *Hydrogen at Scale (H₂ @Scale): Key to a Clean, Economic, and Sustainable Energy System*, The Electrochemical Society Interface **27**, 47 (2018).
- [3] C. Wulf and M. Kaltschmitt, *Hydrogen Supply Chains for Mobility—Environmental and Economic Assessment*, Sustainability **10**, 1699 (2018).
- [4] *Pollution 2.Pdf*.
- [5] M. Pascal, M. Corso, O. Chanel, C. Declercq, C. Badaloni, G. Cesaroni, S. Henschel, K. Meister, D. Haluza, P. Martin-Olmedo, and S. Medina, *Assessing the Public Health Impacts of Urban Air Pollution in 25 European Cities: Results of the Aphekom Project*, Science of The Total Environment **449**, 390 (2013).
- [6] J. Zheng, X. Liu, P. Xu, P. Liu, Y. Zhao, and J. Yang, *Development of High Pressure Gaseous Hydrogen Storage Technologies*, International Journal of Hydrogen Energy **37**, 1048 (2012).
- [7] M. Wietschel, U. Hasenauer, and A. de Groot, *Development of European Hydrogen Infrastructure Scenarios—CO₂ Reduction Potential and Infrastructure Investment*, Energy Policy **34**, 1284 (2006).
- [8] S. Lynch, *Hydrogen Embrittlement Phenomena and Mechanisms*, Corrosion Reviews **30**, (2012).
- [9] C. Julien, J. P. Pereira-Ramos, and A. Momchilov, editors, *New Trends in Intercalation Compounds for Energy Storage* (Springer Netherlands, Dordrecht, 2002).
- [10] H. J. Grabke and E. Riecke, *ABSORPTION AND DIFFUSION OF HYDROGEN IN STEELS*, MATERIALI IN TEHNOLOGIJE **12** (2000).
- [11] C. Spreafico, W. Karim, Y. Ekinici, J. A. van Bokhoven, and J. VandeVondele, *Hydrogen Adsorption on Nanosized Platinum and Dynamics of Spillover onto Alumina and Titania*, The Journal of Physical Chemistry C **121**, 17862 (2017).
- [12] A. Alhussein, J. Capelle, J. Gilgert, S. Dominiak, and Z. Azari, *Influence of Sandblasting and Hydrogen on Tensile and Fatigue Properties of Pipeline API 5L X52 Steel*, International Journal of Hydrogen Energy **36**, 2291 (2011).
- [13] I. M. Robertson, P. Sofronis, A. Nagao, M. L. Martin, S. Wang, D. W. Gross, and K. E. Nygren, *Hydrogen Embrittlement Understood*, Metallurgical and Materials Transactions B **46**, 1085 (2015).
- [14] P. Sofronis, *Viable Mechanisms of Hydrogen Embrittlement—A Review*, in *AIP Conference Proceedings*, Vol. 837 (AIP, Uppsala (Sweden), 2006), pp. 64–70.
- [15] S. K. Dwivedi and M. Vishwakarma, *Hydrogen Embrittlement in Different Materials: A Review*, International Journal of Hydrogen Energy **43**, 21603 (2018).
- [16] R. Gangloff, *Hydrogen Assisted Cracking of High Strength Alloys*, 195 (2003).

- [17] K. Sadananda and A. K. Vasudevan, *Review of Environmentally Assisted Cracking*, Metall and Mat Trans A **42**, 279 (2011).
- [18] R. P. Gangloff, *Critical Issues in Hydrogen Assisted Cracking of Structural Alloys*, **1**, 25 (n.d.).
- [19] H. Leth-Olsen and K. Nisancioglu, *Filiform Corrosion of Aluminium Sheet. I. Corrosion Behaviour of Painted Material*, Corrosion Science **40**, 1179 (1998).
- [20] C. I. Elsner, E. Cavalcanti, O. Ferraz, and A. R. Di Sarli, *Evaluation of the Surface Treatment Effect on the Anticorrosive Performance of Paint Systems on Steel*, Progress in Organic Coatings **48**, 50 (2003).
- [21] T.-H. Nam, J.-H. Lee, S.-R. Choi, J.-B. Yoo, and J.-G. Kim, *Graphene Coating as a Protective Barrier against Hydrogen Embrittlement*, International Journal of Hydrogen Energy **39**, 11810 (2014).
- [22] C. de S. Brandolt, L. C. Noronha, G. E. N. Hidalgo, A. S. Takimi, R. M. Schroeder, and C. de F. Malfatti, *Niobium Coating Applied by HVOF as Protection against Hydrogen Embrittlement of API 5CT P110 Steel*, Surface and Coatings Technology **322**, 10 (2017).
- [23] D. Figueroa and M. J. Robinson, *The Effects of Sacrificial Coatings on Hydrogen Embrittlement and Re-Embrittlement of Ultra High Strength Steels*, Corrosion Science **50**, 1066 (2008).
- [24] J. Zhao, Z. Jiang, and C. S. Lee, *Effects of Tungsten on the Hydrogen Embrittlement Behaviour of Microalloyed Steels*, Corrosion Science **82**, 380 (2014).
- [25] S. Yamaura, Y. Shimpo, H. Okouchi, M. Nishida, O. Kajita, and A. Inoue, *The Effect of Additional Elements on Hydrogen Permeation Properties of Melt-Spun Ni-Nb-Zr Amorphous Alloys**, 4 (n.d.).
- [26] G. Zhang, X. Wang, Y. Xiong, Y. Shi, J. Song, and D. Luo, *Mechanism for Adsorption, Dissociation and Diffusion of Hydrogen in Hydrogen Permeation Barrier of α -Al₂O₃: A Density Functional Theory Study*, International Journal of Hydrogen Energy **38**, 1157 (2013).
- [27] X. Xiang, X. Wang, G. Zhang, T. Tang, and X. Lai, *Preparation Technique and Alloying Effect of Aluminide Coatings as Tritium Permeation Barriers: A Review*, International Journal of Hydrogen Energy **40**, 3697 (2015).
- [28] D. Levchuk, F. Koch, H. Maier, and H. Bolt, *Deuterium Permeation through Eurofer and α -Alumina Coated Eurofer*, Journal of Nuclear Materials **328**, 103 (2004).
- [29] D. Stover, H. P. Buchkremer, and R. Hecker, *HYDROGEN AND DEUTERIUM PERMEATION THROUGH METALLIC AND SURFACE-OXIDIZED CHROMIUM*, 10 (n.d.).
- [30] D. Levchuk, S. Levchuk, H. Maier, H. Bolt, and A. Suzuki, *Erbium Oxide as a New Promising Tritium Permeation Barrier*, Journal of Nuclear Materials **367–370**, 1033 (2007).
- [31] Y. Wu, S. Zhu, T. Liu, F. Li, Y. Zhang, Y. Rao, and Y. Zhang, *Preparation and Properties of Erbium Oxide Films Deposited by Radio Frequency Magnetron Sputtering*, Applied Surface Science **307**, 615 (2014).
- [32] S. Liu, X. Ju, J. Qiu, G. Chen, J. Sun, Y. Xin, and F. Ma, *Tritium-Permeation-Barrier Properties of Erbium Oxide (TPB) Coating on CLAM Steel*, Fusion Engineering and Design **138**, 347 (2019).
- [33] R. Checchetto, L. M. Gratton, A. Miotello, and C. Tosello, *Deuterium Permeation through Sit 2 Thin Film Deposited on Stainless Steel Substrate*, 6 (1997).
- [34] J. Wang, Q. Li, Q.-Y. Xiang, and J.-L. Cao, *Performances of AlN Coatings as Hydrogen Isotopes Permeation Barriers*, Fusion Engineering and Design **102**, 94 (2016).

- [35] V. Nemanič, *Hydrogen Permeation Barriers: Basic Requirements, Materials Selection, Deposition Methods, and Quality Evaluation*, Nuclear Materials and Energy **19**, 451 (2019).
- [36] M. A. Liu, P. E. J. Rivera-Díaz-del-Castillo, J. I. Barraza-Fierro, H. Castaneda, and A. Srivastava, *Microstructural Influence on Hydrogen Permeation and Trapping in Steels*, Materials & Design **167**, 107605 (2019).
- [37] Zhang et al. - 2013 - *Energetics and Diffusion of Hydrogen in Hydrogen p.Pdf*.
- [38] J. P. Chu, J. S. C. Jang, J. C. Huang, H. S. Chou, Y. Yang, J. C. Ye, Y. C. Wang, J. W. Lee, F. X. Liu, P. K. Liaw, Y. C. Chen, C. M. Lee, C. L. Li, and C. Rullyani, *Thin Film Metallic Glasses: Unique Properties and Potential Applications*, Thin Solid Films **520**, 5097 (2012).
- [39] S. Samanta, C. Singh, A. Banerjee, K. Mondal, M. Dutta, and S. B. Singh, *Development of Amorphous Ni-P Coating over API X70 Steel for Hydrogen Barrier Application*, Surface and Coatings Technology **403**, 126356 (2020).
- [40] V. Nemanič, P. J. McGuinness, N. Daneu, B. Zajec, Z. Siketić, and W. Waldhauser, *Hydrogen Permeation through Silicon Nitride Films*, Journal of Alloys and Compounds **539**, 184 (2012).
- [41] M. Ichiba, K. Takai, and J. Sakai, *Effects of Test Conditions on Corrosion Reactions and Hydrogen Absorption in Hydrogen Embrittlement Tests Using an Ammonium Thiocyanate Solution*, ISIJ International **56**, 397 (2016).
- [42] R. N. Parkins, W. K. Blanchard, and B. S. Delanty, *Transgranular Stress Corrosion Cracking of High-Pressure Pipelines in Contact with Solutions of Near Neutral PH*, CORROSION **50**, 394 (1994).
- [43] C. W. Chu, J. S. C. Jang, G. J. Chen, and S. M. Chiu, *Characteristic Studies on the Zr-Based Metallic Glass Thin Film Fabricated by Magnetron Sputtering Process*, Surface and Coatings Technology **202**, 5564 (2008).
- [44] C. W. Chu, J. S. C. Jang, S. M. Chiu, and J. P. Chu, *Study of the Characteristics and Corrosion Behavior for the Zr-Based Metallic Glass Thin Film Fabricated by Pulse Magnetron Sputtering Process*, Thin Solid Films **517**, 4930 (2009).
- [45] A. Obeydavi, *Microstructure, Mechanical Properties and Corrosion Performance of Fe₄₄Cr₁₅Mo₁₄Co₇C₁₀B₅Si₅ Thin Film Metallic Glass Deposited by DC Magnetron Sputtering*, 17 (2020).
- [46] A. Inoue, *STABILIZATION OF METALLIC SUPERCOOLED LIQUID AND BULK AMORPHOUS ALLOYS* p, 28 (n.d.).
- [47] A. Takeuchi and A. Inoue, *Classification of Bulk Metallic Glasses by Atomic Size Difference, Heat of Mixing and Period of Constituent Elements and Its Application to Characterization of the Main Alloying Element*, MATERIALS TRANSACTIONS **46**, 2817 (2005).
- [48] A. Billard and F. Perry, *Pulvérisation cathodique magnétron*, 23 (2005).
- [49] F. Sanchette, A. Billard, and C. Frantz, *Mechanically Reinforced and Corrosion-Resistant Sputtered Amorphous Aluminium Alloy Coatings*, Surface and Coatings Technology **98**, 1162 (1998).
- [50] O. P. Rachek, *X-Ray Diffraction Study of Amorphous Alloys Al-Ni-Ce-Sc with Using Ehrenfest's Formula*, Journal of Non-Crystalline Solids **352**, 3781 (2006).
- [51] G. Zhao, R. Wang, S. Liu, T. Wang, D. Wu, Y. Zhang, J. Chen, and Y. Zou, *Microstructure Analysis of Element W in Improving the Ni-P Deposit Thermal Stability*, Journal of Materials Research and Technology **9**, 5474 (2020).
- [52] H. C. Kim, N. D. Theodore, K. S. Gadre, J. W. Mayer, and T. L. Alford, *Investigation of Thermal Stability, Phase Formation, Electrical, and Microstructural Properties of Sputter-Deposited Titanium Aluminide Thin Films*, Thin Solid Films **460**, 17 (2004).

- [53] O. N. Senkov and M. D. Uchic, *Microstructure Evolution during Annealing of an Amorphous TiAl Sheet*, *Materials Science and Engineering: A* **340**, 216 (2003).
- [54] *Al-Ti-W Article.Pdf*.
- [55] B. R. Braeckman and D. Depla, *On the Amorphous Nature of Sputtered Thin Film Alloys*, *Acta Materialia* **109**, 323 (2016).
- [56] G. Abadias, E. Chason, J. Keckes, M. Sebastiani, G. B. Thompson, E. Barthel, G. L. Doll, C. E. Murray, C. H. Stoessel, and L. Martinu, *Review Article: Stress in Thin Films and Coatings: Current Status, Challenges, and Prospects*, *Journal of Vacuum Science & Technology A: Vacuum, Surfaces, and Films* **36**, 020801 (2018).
- [57] J.-C. Chang, J.-W. Lee, B.-S. Lou, C.-L. Li, and J. P. Chu, *Effects of Tungsten Contents on the Microstructure, Mechanical and Anticorrosion Properties of Zr–W–Ti Thin Film Metallic Glasses*, *Thin Solid Films* **584**, 253 (2015).
- [58] N. Radić, A. Tonejc, M. Milun, P. Pervan, J. Ivkov, and M. Stubičar, *Preparation and Structure of AlW Thin Films*, *Thin Solid Films* **317**, 96 (1998).
- [59] B.-S. Lou, Y.-C. Yang, J.-W. Lee, and L.-T. Chen, *Biocompatibility and Mechanical Property Evaluation of Zr-Ti-Fe Based Ternary Thin Film Metallic Glasses*, *Surface and Coatings Technology* **320**, 512 (2017).
- [60] A. C. Crossland, G. E. Thompson, C. J. E. Smith, H. Habazaki, K. Shimizu, and P. Skeldon, *Formation of Manganese-Rich Layers during Anodizing of Al–Mn Alloys*, *Corrosion Science* **41**, 2053 (1999).
- [61] A. C. Crossland, G. E. Thompson, J. Wan, H. Habazaki, K. Shimizu, P. Skeldon, and G. C. Wood, *The Composition and Morphology of Anodic Films on Al-Mo Alloys*, *J. Electrochem. Soc.* **144**, 847 (1997).
- [62] D. Guo and C. T. Kwok, *A Corrosion Study on W-Cu Alloys in Sodium Chloride Solution at Different PH*, *Journal of Materials Science & Technology* **64**, 38 (2021).
- [63] A. Królikowski, E. Płońska, A. Ostrowski, M. Donten, and Z. Stojek, *Effects of Compositional and Structural Features on Corrosion Behavior of Nickel–Tungsten Alloys*, *J Solid State Electrochem* **13**, 263 (2009).
- [64] N. Padhy, S. Ningshen, and U. Kamachi Mudali, *Electrochemical and Surface Investigation of Zirconium Based Metallic Glass Zr₅₉Ti₃Cu₂₀Al₁₀Ni₈ Alloy in Nitric Acid and Sodium Chloride Media*, *Journal of Alloys and Compounds* **503**, 50 (2010).
- [65] N. Shakibi Nia, J. Creus, X. Feaugas, and C. Savall, *Influence of Metallurgical Parameters on the Electrochemical Behavior of Electrodeposited Ni and Ni–W Nanocrystalline Alloys*, *Applied Surface Science* **370**, 149 (2016).
- [66] M. Lagarde, A. Billard, J. Creus, X. Feaugas, J. L. Grosseau-Poussard, S. Touzain, and C. Savall, *Electrochemical Behavior of Ni W Alloys Obtained by Magnetron Sputtering*, *Surface and Coatings Technology* **352**, 581 (2018).
- [67] Y. Zheng, Y. Jiao, A. Vasileff, and S.-Z. Qiao, *The Hydrogen Evolution Reaction in Alkaline Solution: From Theory, Single Crystal Models, to Practical Electrocatalysts*, *Angew. Chem. Int. Ed.* **57**, 7568 (2018).
- [68] W. C. Luu and J. K. Wu, *The Influence of Microstructure on Hydrogen Transport in Carbon Steels*, *Corrosion Science* **38**, 239 (1996).
- [69] N. Parvathavarthini, S. Saroja, R. K. Dayal, and H. S. Khatak, *Studies on Hydrogen Permeability of 2.25% Cr–1% Mo Ferritic Steel: Correlation with Microstructure*, *Journal of Nuclear Materials* **288**, 187 (2001).

Figures

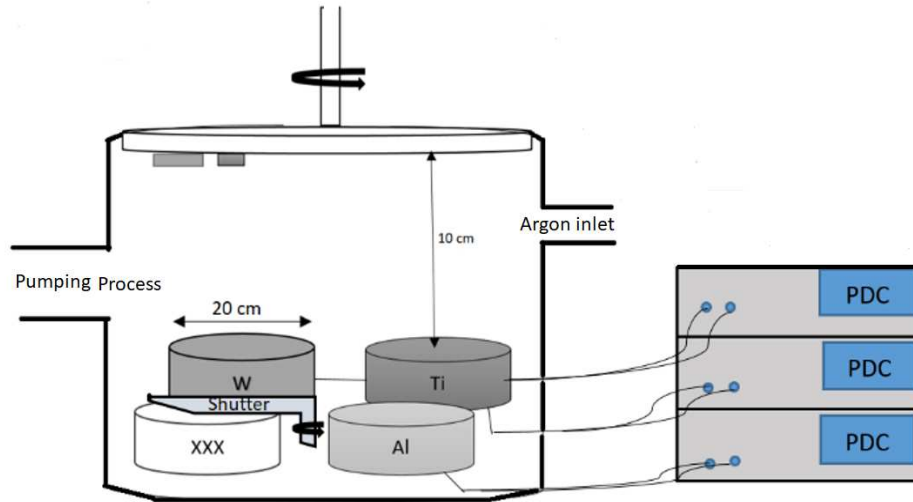


Fig. 1. Schematic view of the PVD machine used for Al-Ti-W thin film deposition.

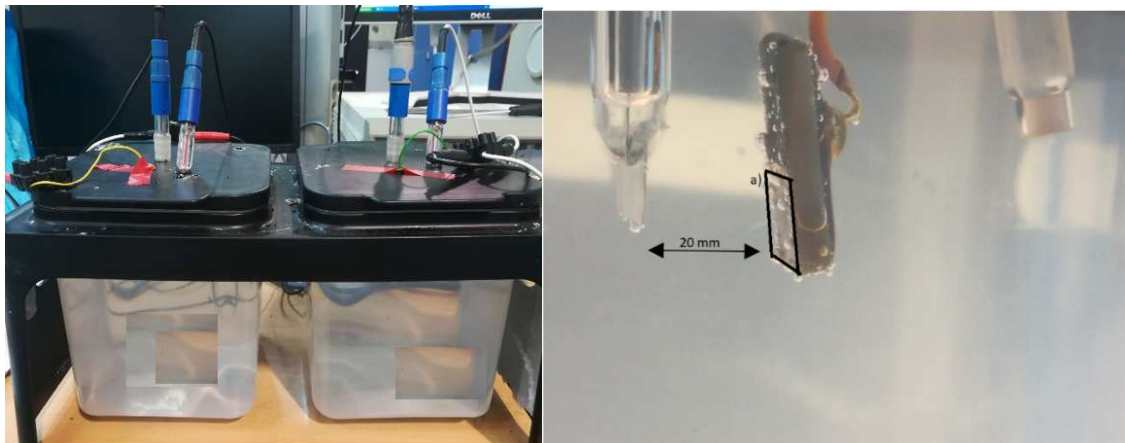


Fig. 2. Hydrogen charging in NS4 electrochemical cell.

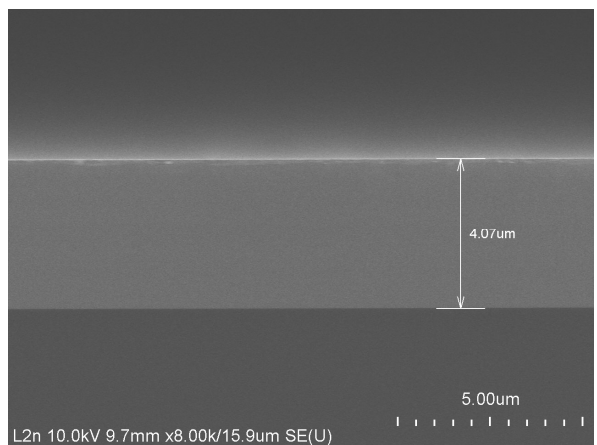
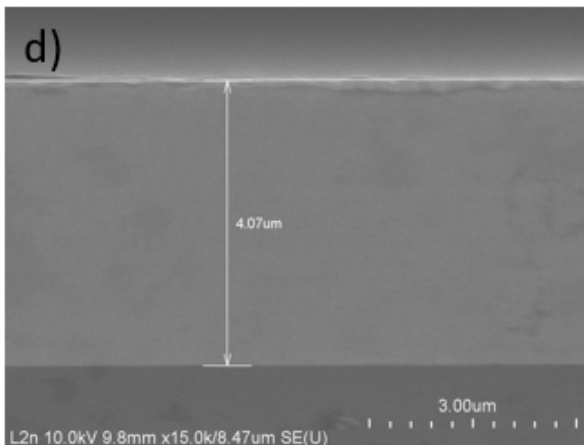
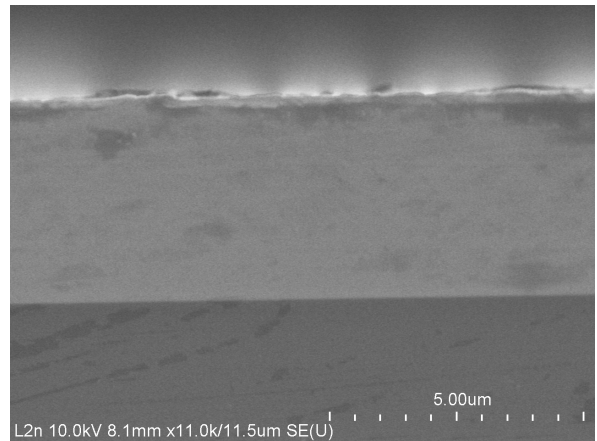
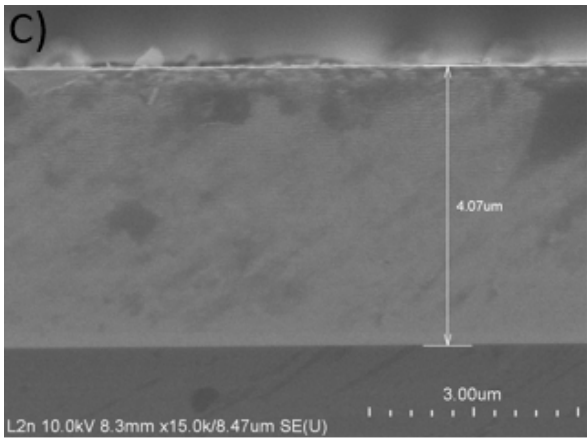
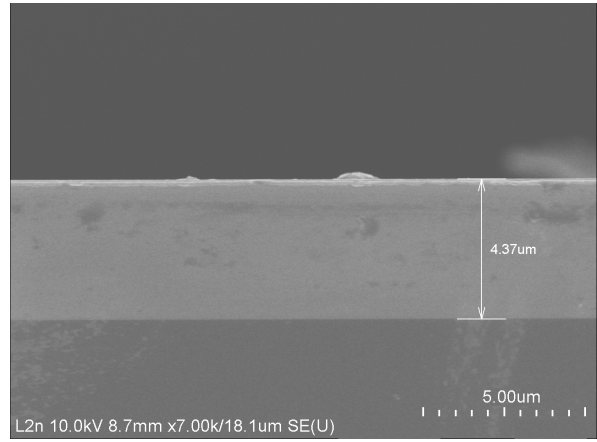
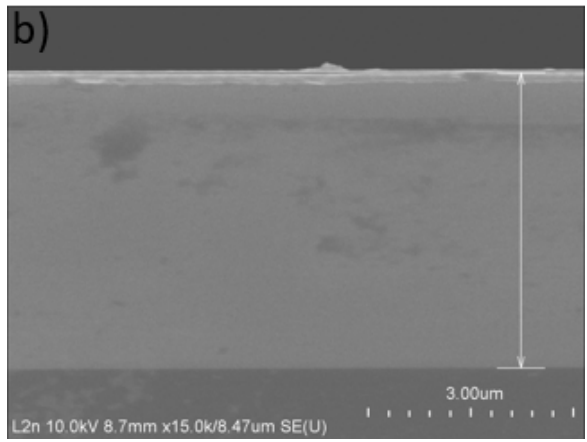
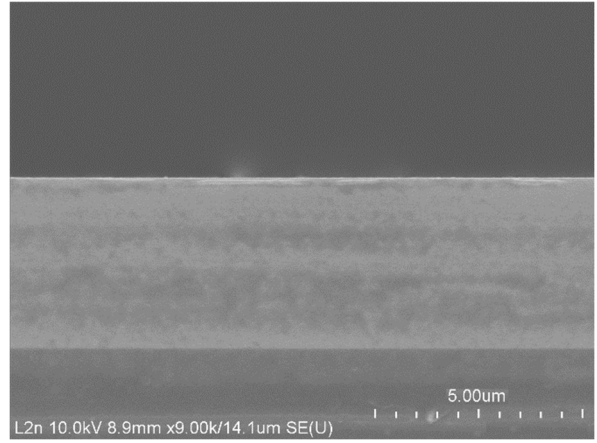
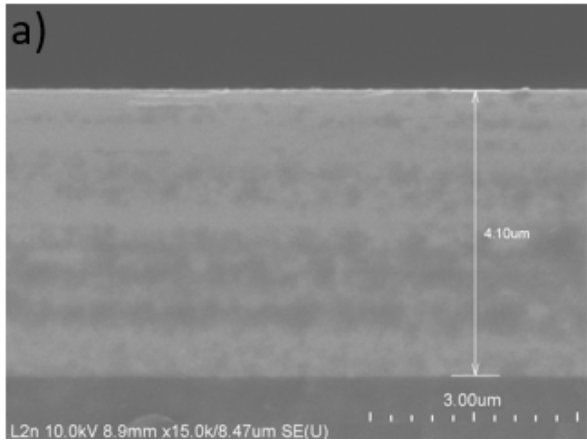


Fig. 4. Cross sectional SEM images of Al-Ti thin films containing: a) 0 % W, b) 4 % W, c) 11 % W, and d) 17 % W.

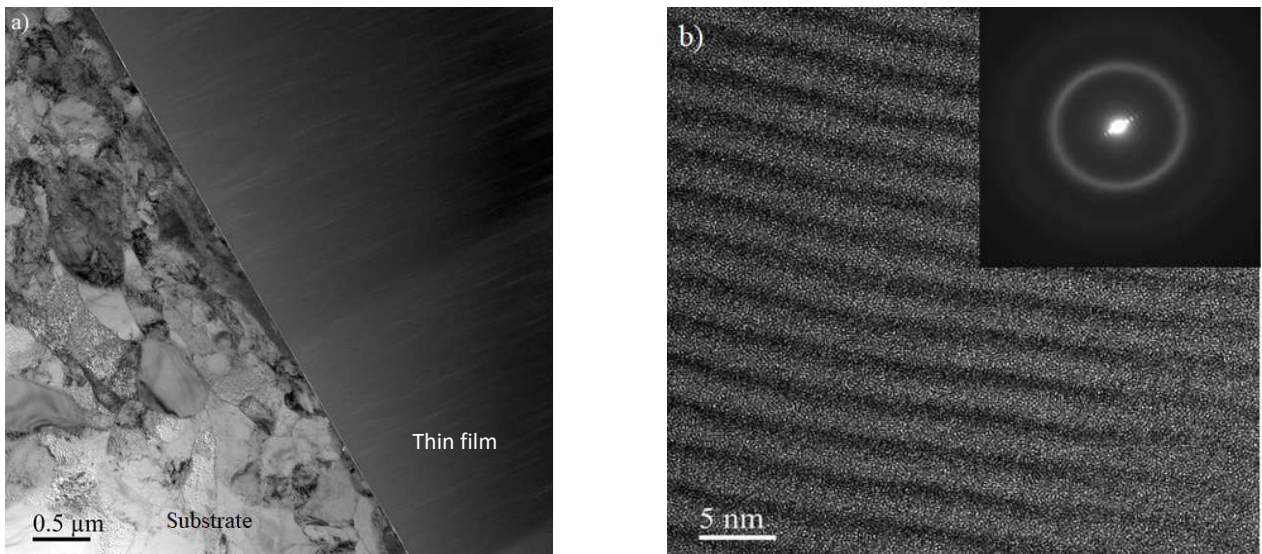


Fig. 5. a) BFTEM film/substrate image and b) HRTEM and SAED images of Al₄₅Ti₃₈W₁₇ thin film.

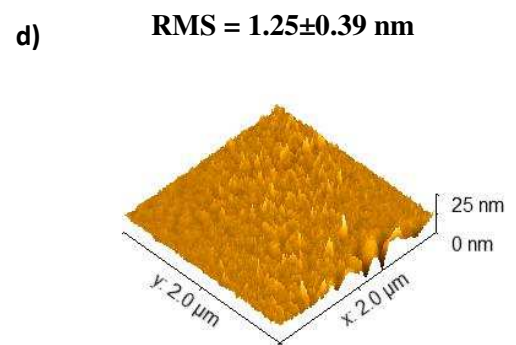
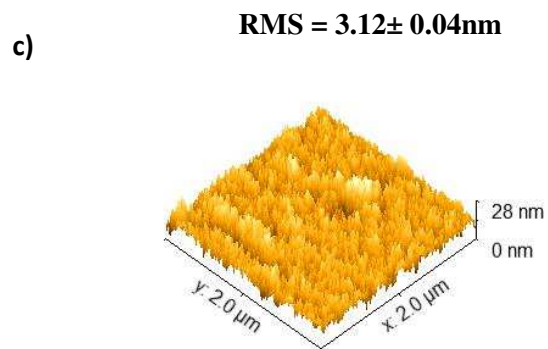
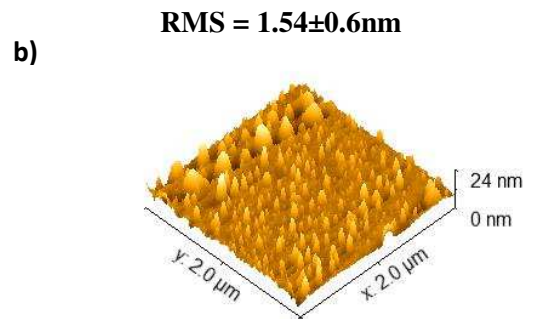
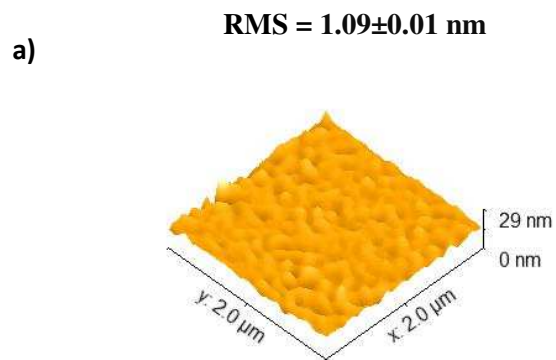


Fig. 6. AFM images of Al-Ti thin films containing: a) 0 % W, b) 4 % W, c) 11 % W and d) 17 % W.

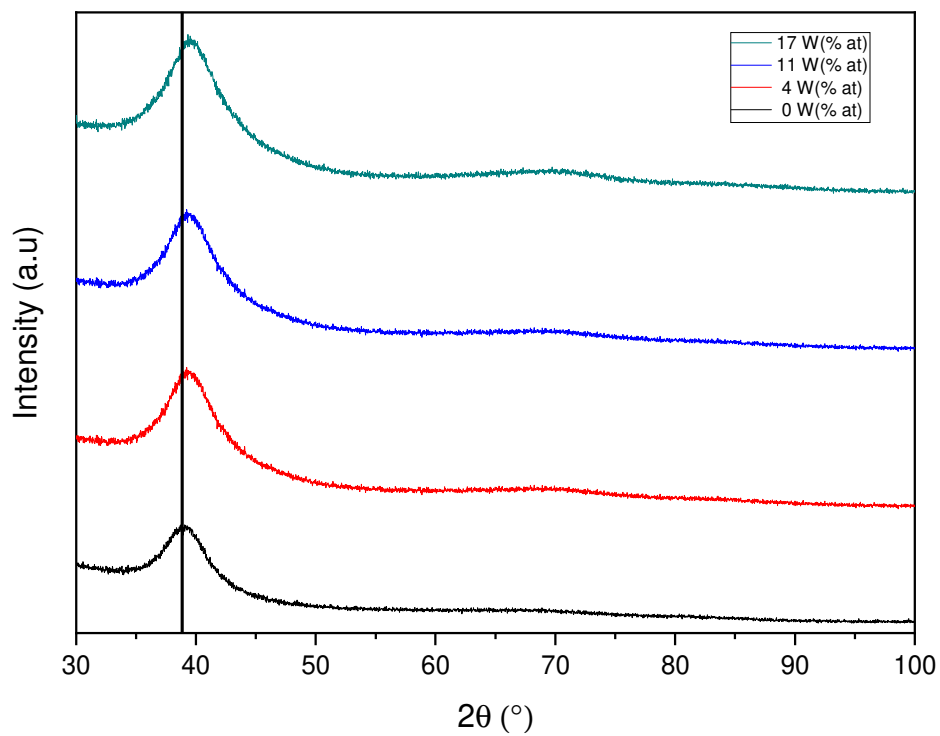


Fig. 7. X-ray diffraction patterns of Al-Ti-(W) thin films.

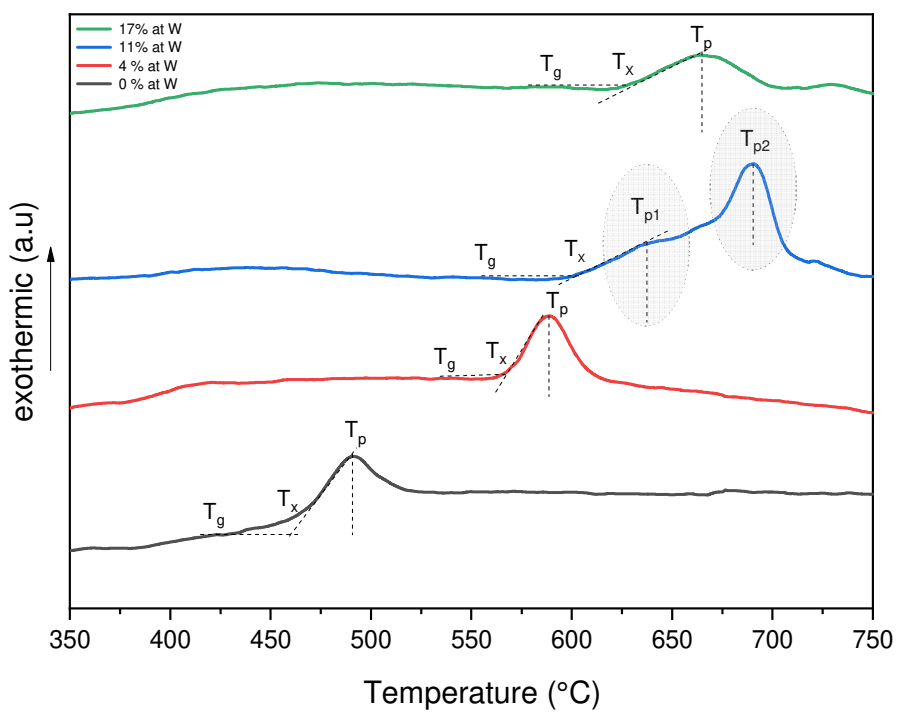


Fig. 8. DSC thermograms of the TiAl-(W) thin films.

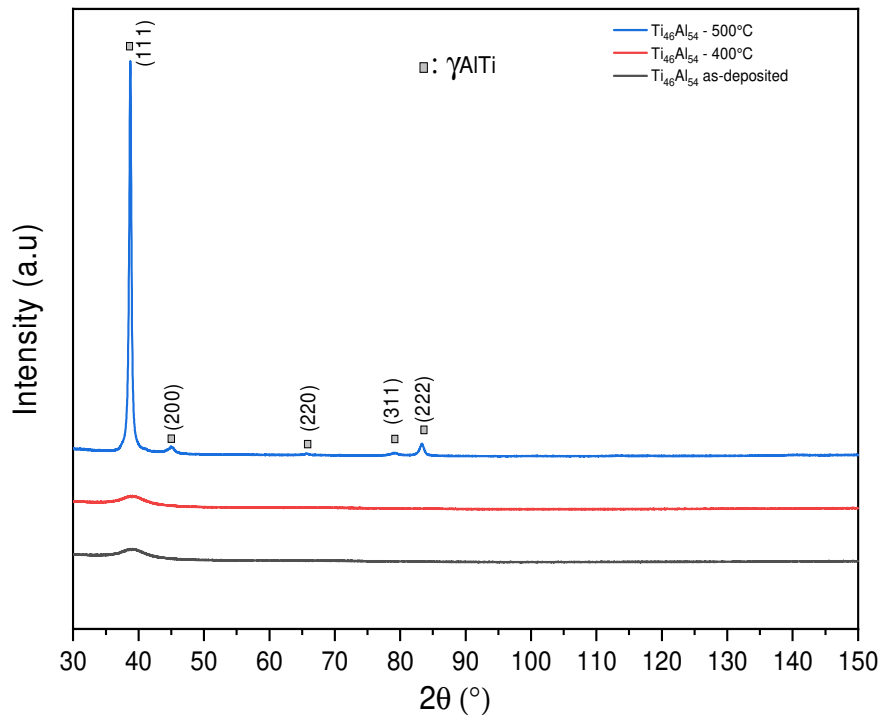


Fig. 9. XRD patterns showing the structure evolution of $Al_{54}Ti_{46}$ thin film as a function of annealing temperature.

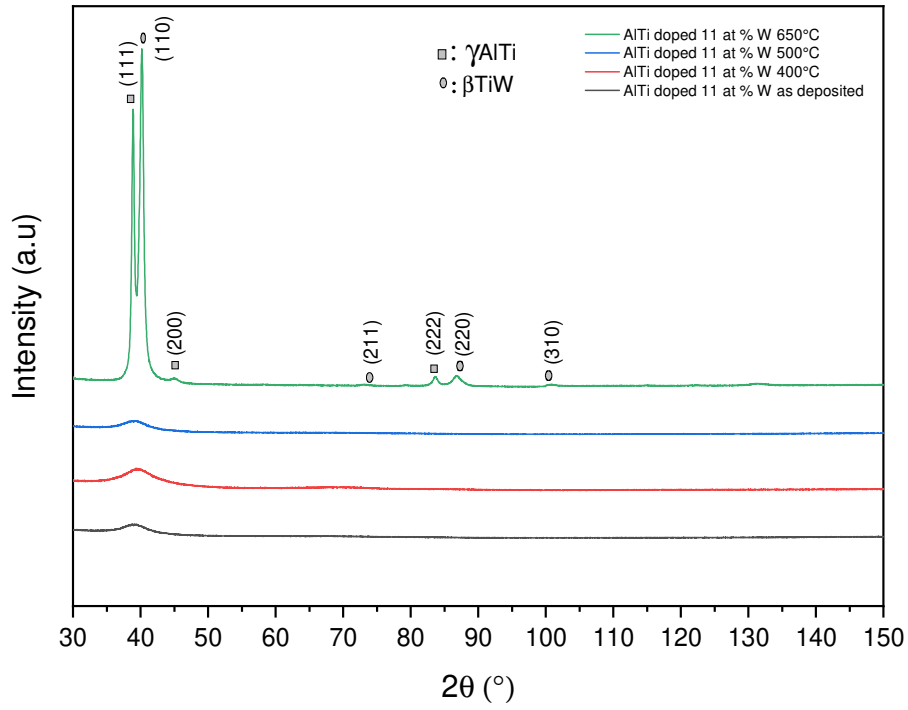


Fig. 10. XRD patterns showing the structure evolution of $Al_{49}Ti_{40}W_{11}$ thin film as a function of annealing temperature.

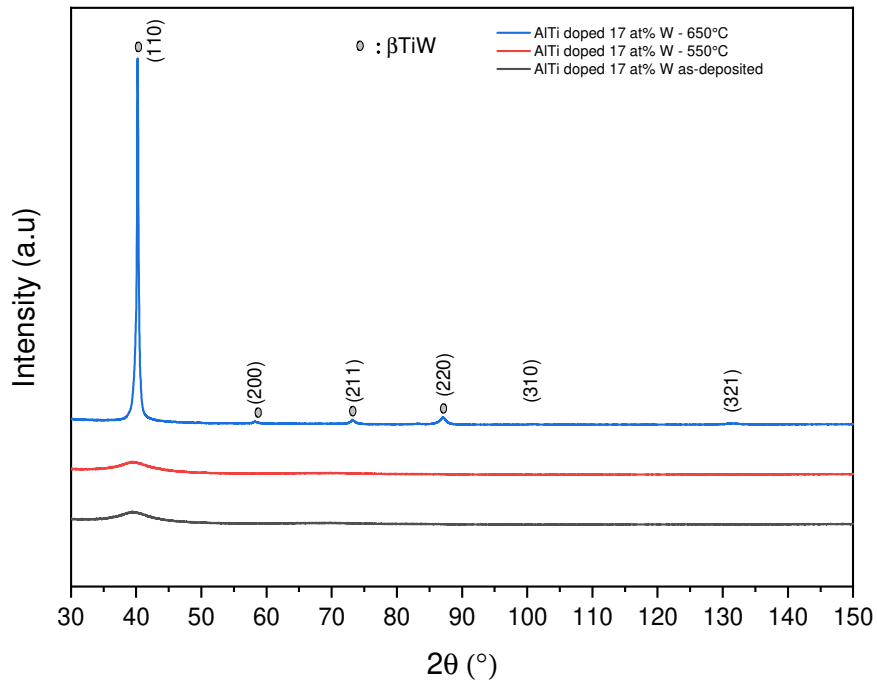


Fig. 11. XRD patterns showing the structure evolution of $Al_{45}Ti_{38}W_{17}$ thin film as a function of annealing temperature.

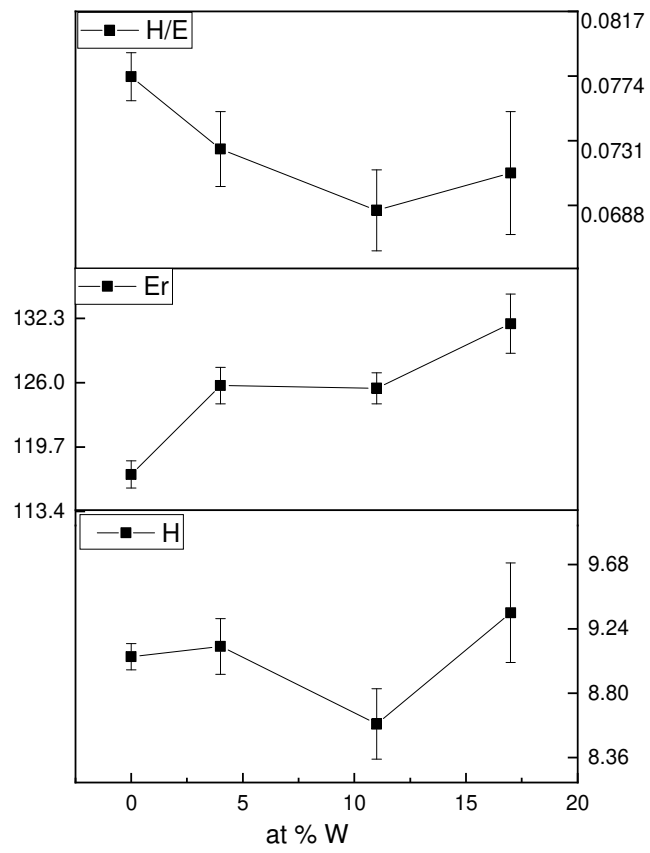


Fig. 12. H, Er and H/Er of *Al-Ti-(W)* thin films.

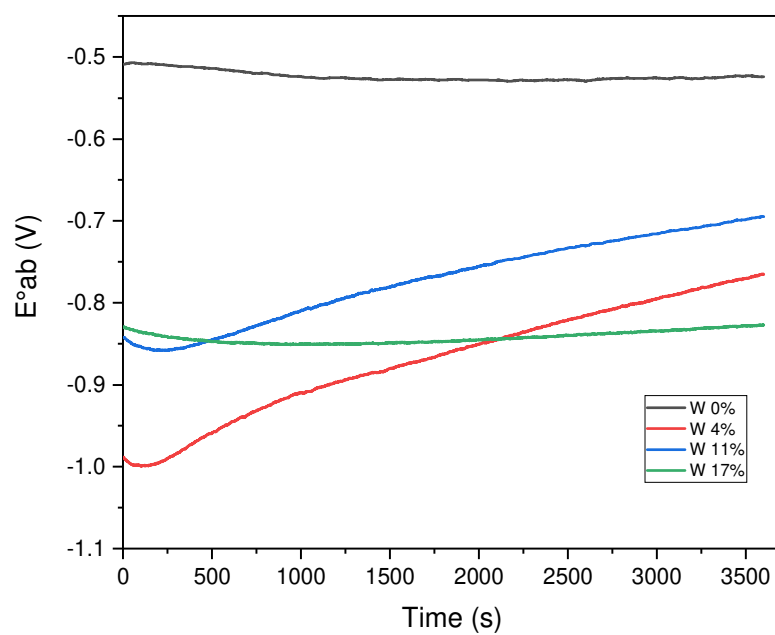


Fig. 13. Evolution of open circuit potential as a function of exposure time.

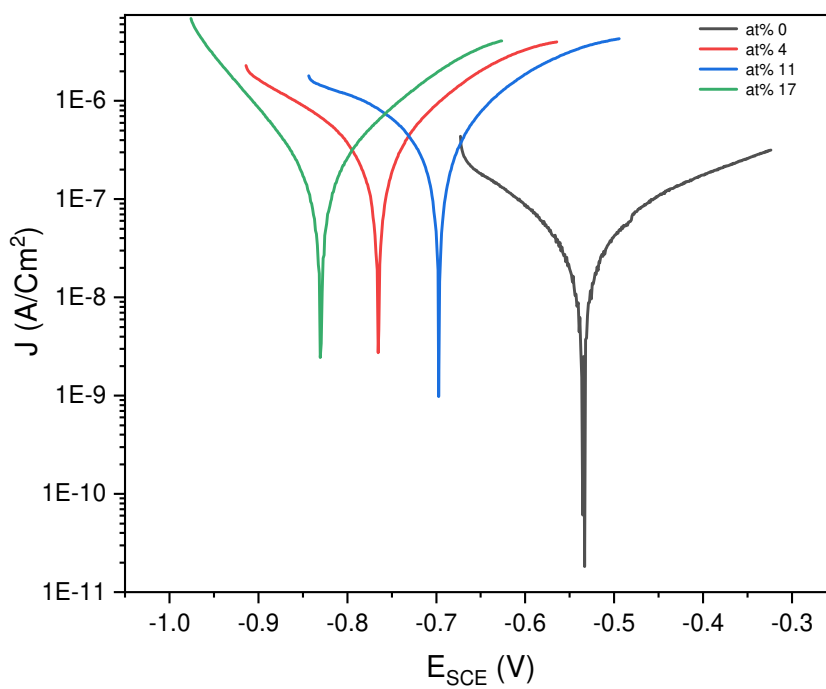


Fig. 14. Polarization curves of Al-Ti-(W) thin films.

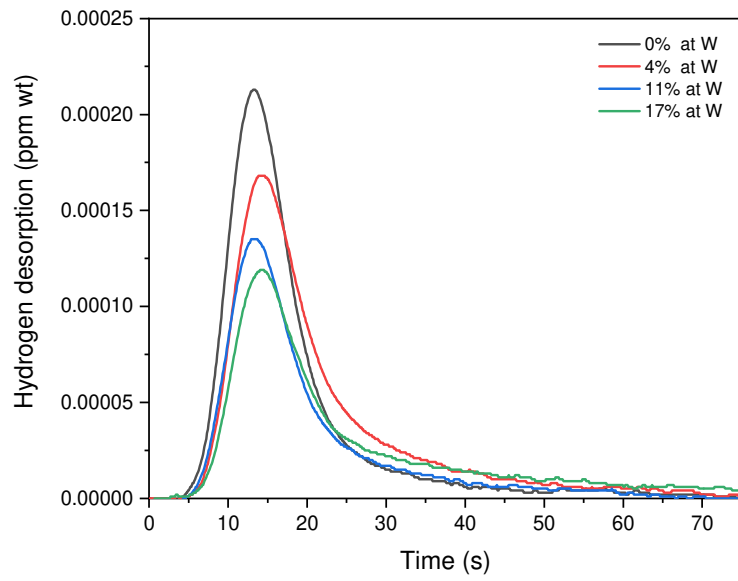


Fig. 15. Thermal desorption spectroscopy curves of Al-Ti-(W) thin films.

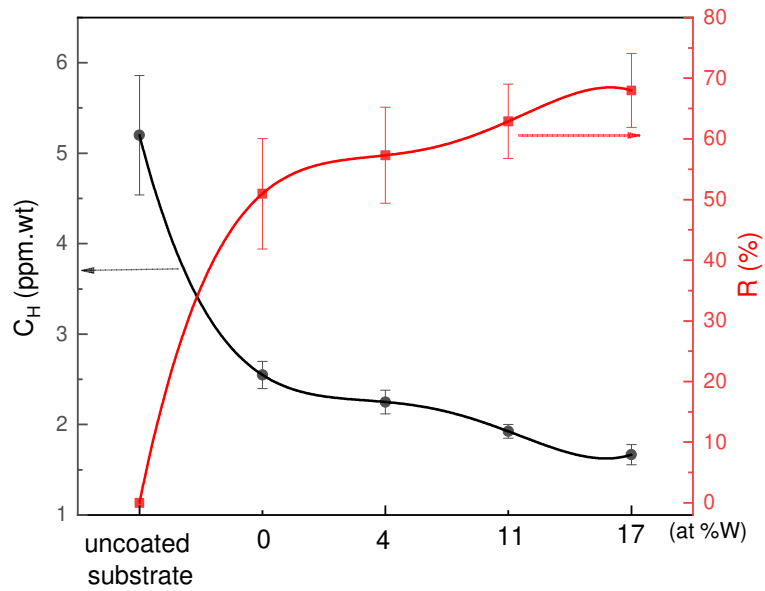


Fig. 16. Hydrogen concentration and Reduction factor in different Al-Ti-(W) thin films.

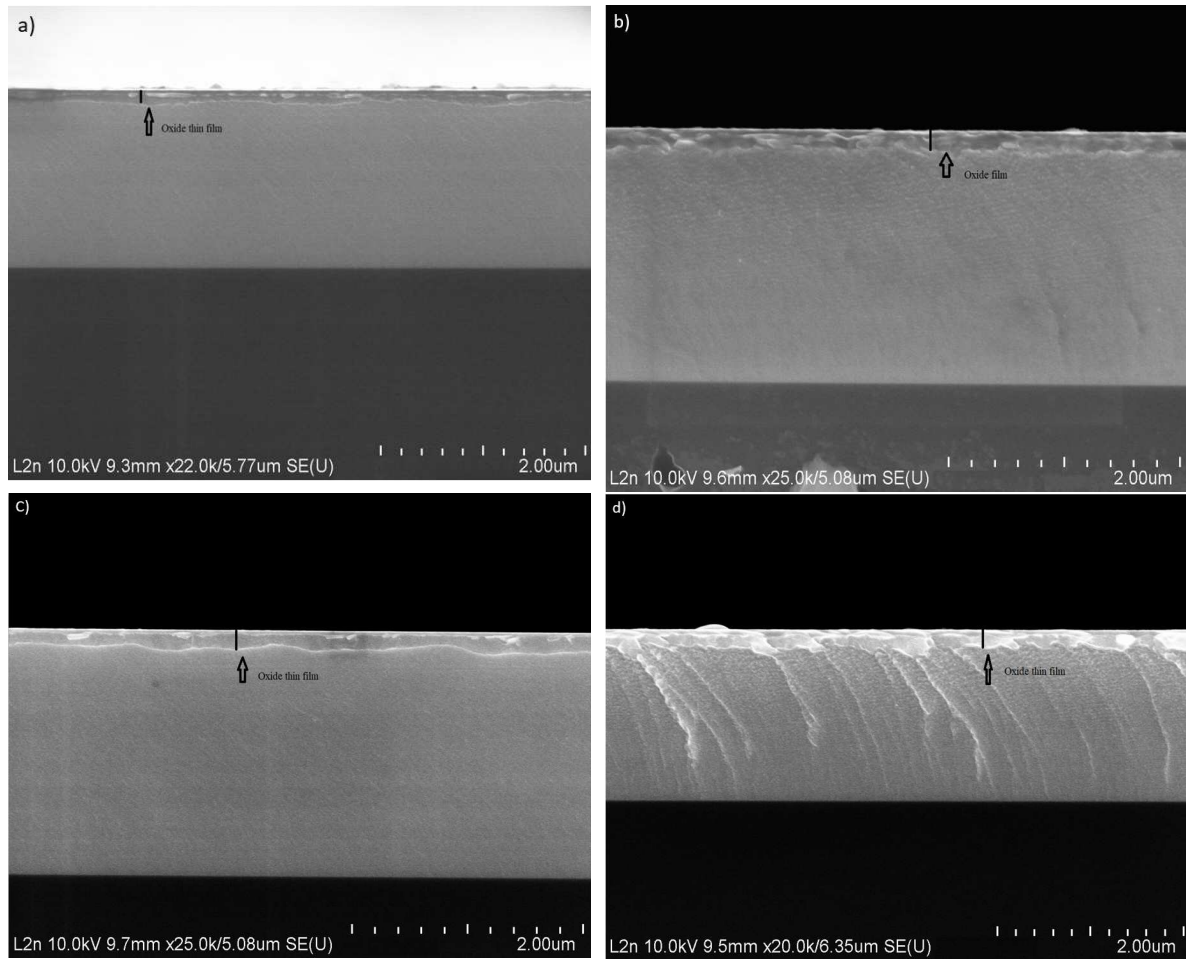


Fig. 17. Cross sectional SEM images of Al-Ti thin films containing: a) 0 % W, b) 4 % W, c) 11 % W and d) 17 % W after hydrogen chemical charging.

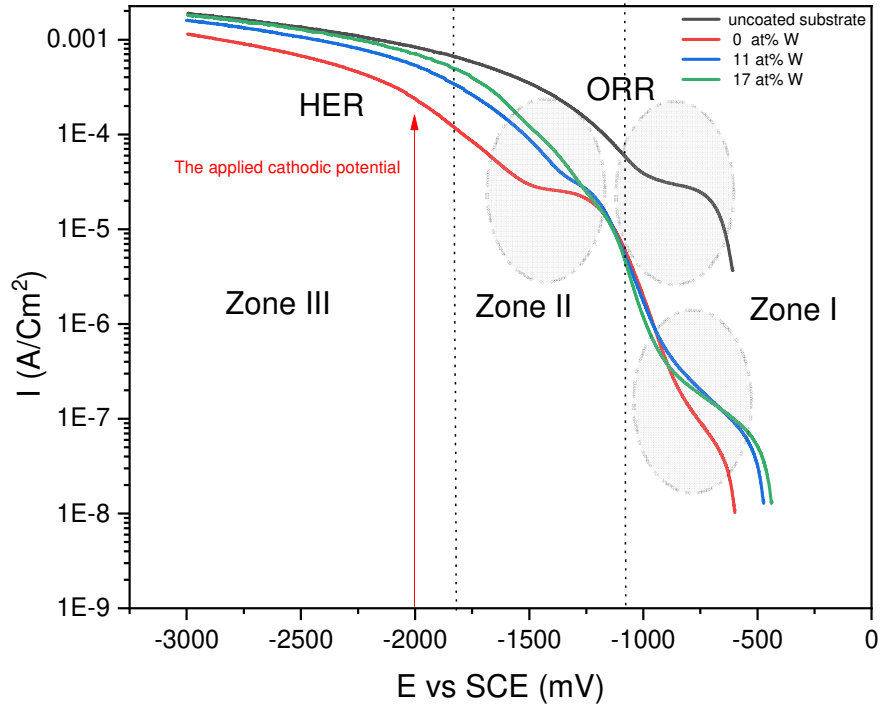
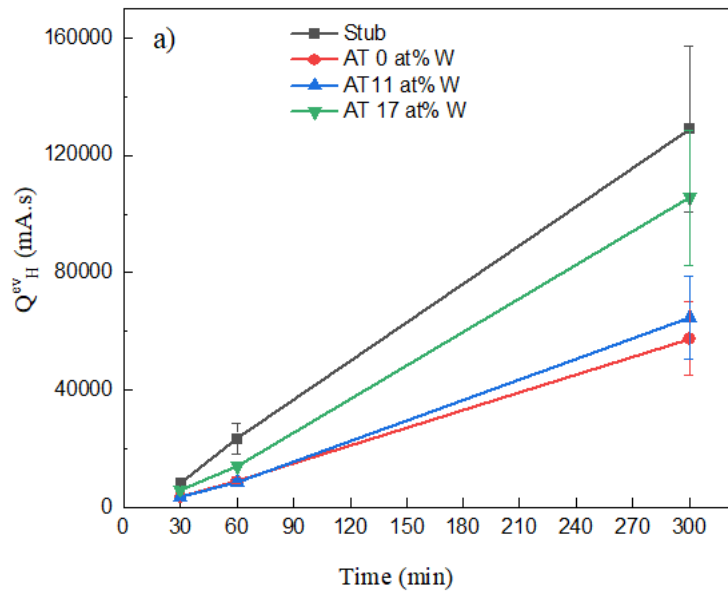


Fig. 18. Cathodic polarization of 100C6 steel and AlTi-(W) thin films.



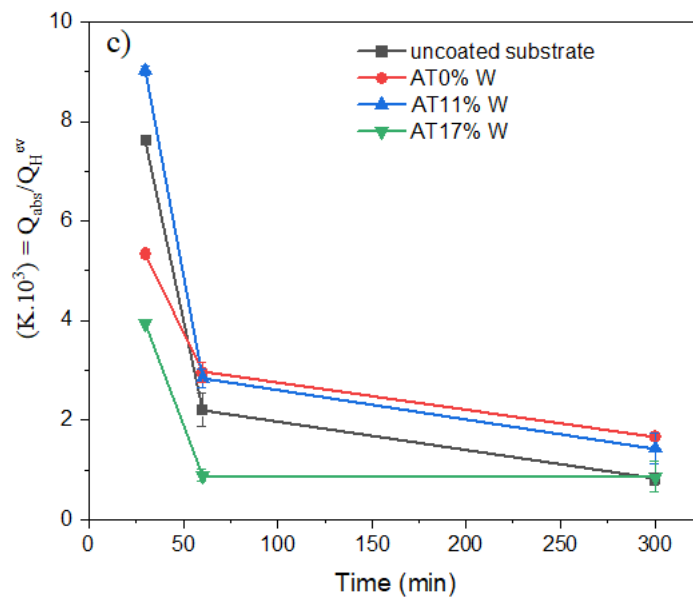
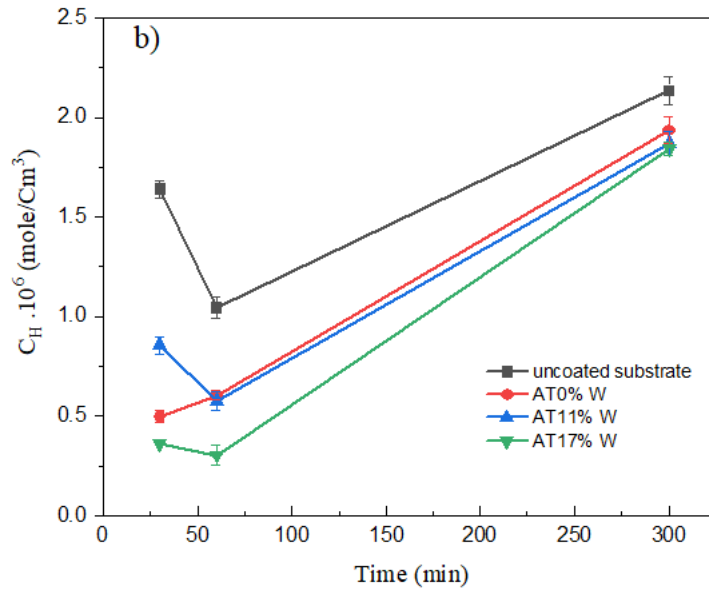


Fig. 19. a) $Q_{generated}$, b) C_H , and c) K coefficient for substrate and Al-Ti-(W) thin films at different exposure times.

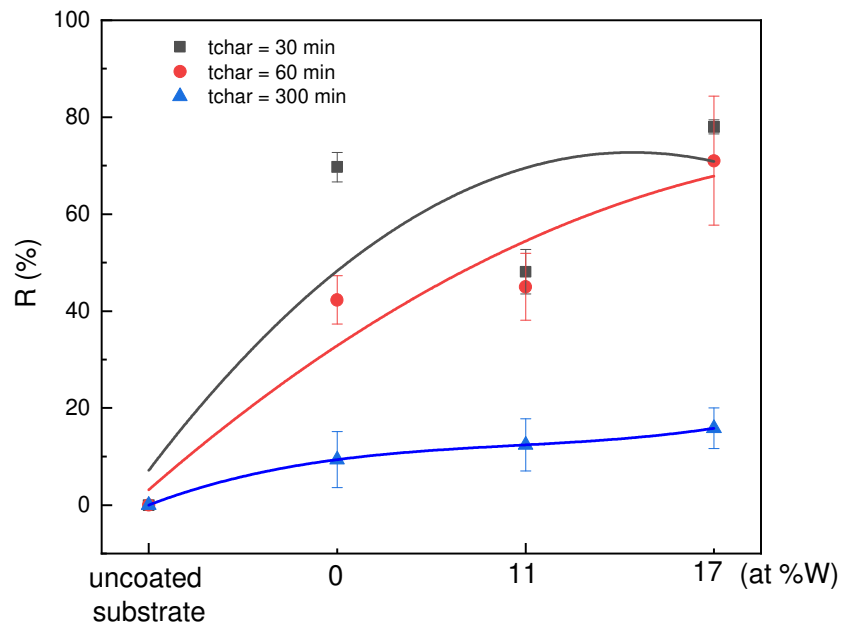


Fig. 20. Reduction factor R after hydrogen electrochemical charging for substrate and Al-Ti-(W) thin films.

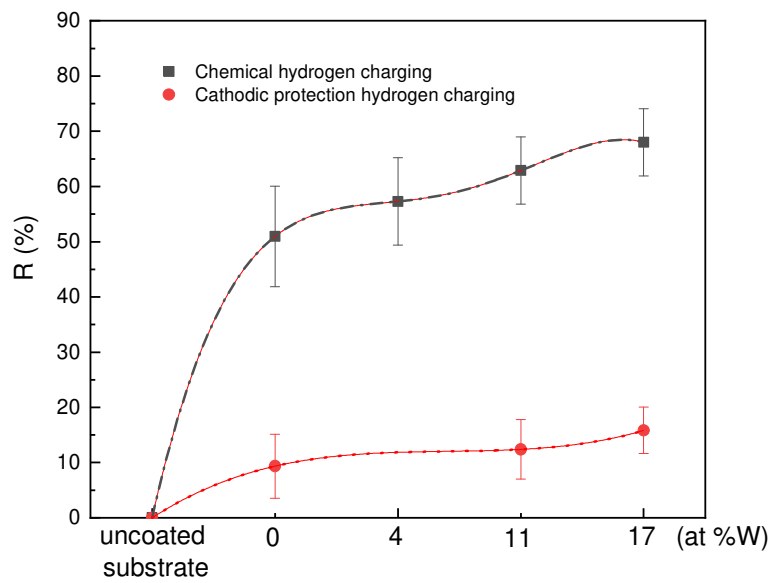


Fig. 21. Evolution of R factor as a function of W content in different hydrogen charging methods.

Tables

Table 1. Chemical composition of the 100C6 Steel substrate.

Chemical element	Fe	Cr	Mn	Si
Wt (%)	97.91	1.37	0.40	0.28

Table 2. Chemical composition of NS4 Solution, pH = 7.4 at room temperature.

Chemical composition of NS4	Concentration (mg/l)
Sodium hydrogen carbonate: NaHCO ₃	483
Potassium chloride: KCl	122
Calcium chloride dehydrate: CaCl ₂ .2H ₂ O	181
Magnesium sulfate heptahydrate: MgSO ₄ .7H ₂ O	131

Table 3. Deposition parameters and composition of Al-Ti-W thin films.

Current Intensity (A)			Deposition rate (μm.h⁻¹)	Deposition time (min)	Composition (at. %)				
Al	Ti	W			Al	Ti	W	$\frac{Ti}{Al}$	$\frac{W}{(W + Ti + Al)}$
		-	1.35	176	54.3±2.1	45.7±1.8	-	0.84	0
1.66	2.7	0.2	1.41	170	50.8±1.6	45.3±1.5	3.8 ± 0.6	0.89	0.038
		0.5	1.61	148	48.9±1.3	39.3±1.1	11.7±1.5	0.80	0.11
		0.8	1.75	138	45±1.1	37.5±1.1	17.5±2.6	0.83	0.17

Table 4. Atomic radii and atomic pair difference of Al, Ti and W elements.

<i>Chemical element</i>	<i>Al</i>	<i>Ti</i>	<i>W</i>	
<i>Atomic radius (pm)</i>	143	147	137	
<i>Atomic pair difference (%)</i>	<i>Al</i>	–	2.72	4.37
	<i>Ti</i>	2.8	–	7.3
	<i>W</i>	2.78	6.8	–

Table 5. Heat of mixing of atomic pairs.

<i>Atomic pair</i>	<i>W-Ti</i>	<i>W-Al</i>	<i>Ti-Al</i>
<i>Heat of mixing ΔH_{mix} (KJ/mole)</i>	-6	-2	-30

Table 6. Interatomic distance between the closest atomic neighbors of Al-Ti-(W) thin films.

<i>W content (at.%)</i>	0	4	11	17
$\Theta(^{\circ})$	19.42	19.7	19.7	19.8
$r(\text{\AA})$	2.85	2.8	2.8	2.79

Table 7. DSC experimental conditions, Tx, Tp and Tg temperatures of AlTi-(W) thin films.

<i>W</i> percentage in TiAl film (at %)	0	4	11	17
Empty Crucible (mg)	206.7	209	206.7	206.4
Crucible containing the coating (mg)	210.8	215.5	214.2	214.3
Heating rate (K/min)			15	
Cooling rate (K/min)			30	
Ar gas flow (ml/min)			200	
Heating temperature range (C°)			25-800	
Tp (°C)	490	588	637/690	665
Tg (°C)	423	540	556	595
Tx (°C)	466	567	600	630
ΔT (°C)	43	27	44	35

Table 8. Mechanical proprieties and residual stress of Al-Ti-(W) thin films.

<i>W</i> content (at.%)	0	4	11	17
σ_{res} (MPa)	45±3	-5±3	-24±5	-14±2
<i>H</i>(GPa)	9.05±0.09	9.12±0.19	8.59±0.24	9.35±0.34
<i>E_r</i>(GPa)	117±1.33	125.72±1.79	125.46±1.52	131.79±2.91
<i>H/E_r</i>	0.077	0.072	0.068	0.070

Table 9. Electrochemical parameters of corrosion in NS4 aqueous solution.

<i>W content (at %)</i>	0	4	11	17
J_{corr} (nA/cm ²)	54	260	580	162
E_{corr} (V)	-0.53	-0.76	-0.69	-0.83
β_c (V/dec.)	0.215	0.184	0.326	0.105
β_a (V/dec.)	0.265	0.121	0.221	0.115
R (k Ω .cm ²)	954	121.9	98.60	147.11

Table 10. Hydrogen concentration (C_H) after chemical charging in an ammonium thiocyanate solution.

Sample type	C_H (ppm.Wt)
Uncoated samples before hydrogen charging	0.1
Uncoated samples after hydrogen charging	5.2±0.66
Coated sample / Al-Ti	2.55±0.15
Coated sample/Al-Ti-W (4%)	2.25±0.13
Coated sample/ Al-Ti-W (11%)	1.92±0.075
Coated sample/ Al-Ti-W (17%)	1.66±0.11

Table 11. Measurement values obtained from hydrogen electrochemical charging of Al-Ti-(W) thin films for different exposure times.

	W (at %)	T_{charg} (min)	I_{cath} (mA/Cm ²)	Q_{an.ref} (mA .s)	<Q_{created}> (mA .s)	<Q_{dis}> (mA.s)	<K>.10³	<C_H>.10⁶ (mol/cm ³)
Uncoated 100C6 Steel	-	30	- 4.9	5.16	8300.3	74.11	7.629	1.640
		60	-5		18313	45.49	2.203	1.045
		300	-5.7		100783	87.64	0.818	2.136
Coated substrate	0	30	-2.2	10.97	3599.97	23.7	5.34	0.498
		60	-2.2		7869.36	25.81	2.96	0.603
		300	-2.5		44939.7	85.74	1.66	1.936
	11	30	-2.4	3.65	3657.9	31.524	9.02	0.855
		60	-1.8		7817	21.75	2.83	0.574
		300	-3.5		50547	75.87	1.42	1.871
	17	30	-4.3	10.11	3545.9	29.70	3.94	0.361
		60	-4.3		13214	34.28	0.88	0.303
		300	-5.1		82456.4	81.43	0.86	1.844

Graphical Abstract

Hydrogen barrier thin film

Influence of tungsten on the AlTiW thin film behavior

